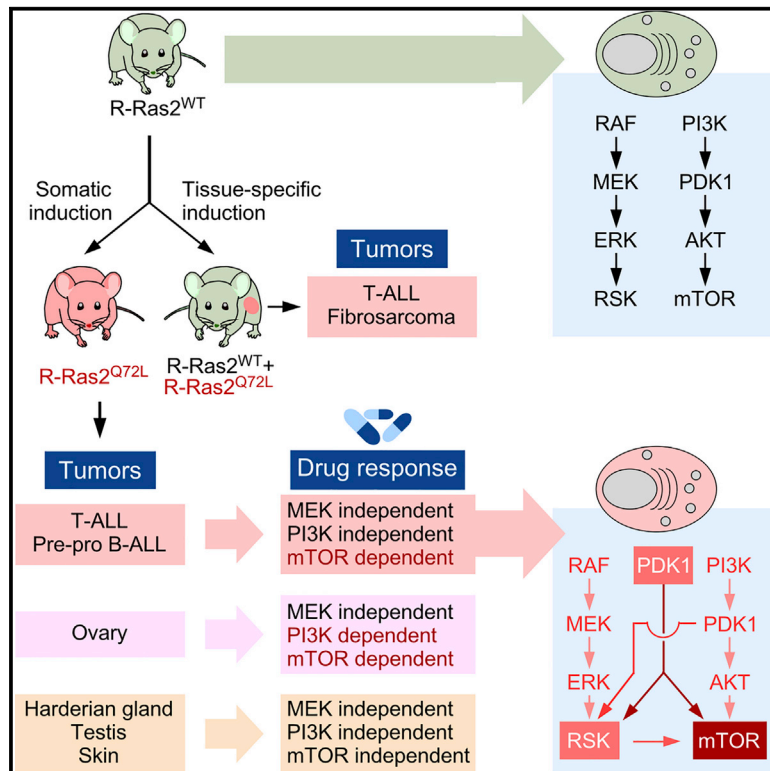# Cell Reports

A hotspot mutation targeting the R-RAS2 GTPase acts as a potent oncogenic driver in a wide spectrum of tumors

Graphical abstract

Authors

Isabel Fernández-Pisonero,
Laura Clavaín, Javier Robles-Valero, ...,
Mercedes Dosil, Balbino Alarcón,
Xosé R. Bustelo

Correspondence

xbustelo@usal.es

In brief

Fernández-Pisonero et al. demonstrate, using a mouse model, that the Q72L mutation of *RRAS2* found in human tumors acts as a potent oncogenic driver in a diverse spectrum of tissues. This activity is quite different from the signaling and tumor types typically induced by classical RAS oncoproteins.

Highlights

- *RRAS2*^{Q72L} is a long-tail hotspot mutation identified in pan-cancer data

- R-RAS2^{Q72L} behaves as a potent oncogenic driver for a large spectrum of tumors

- R-RAS2^{Q72L} triggers cell-type-specific pathobiological programs

- R-RAS2^{Q72L}-driven tumors show drug vulnerabilities of potential clinical interest

CellPress

Article

A hotspot mutation targeting the R-RAS2 GTPase acts as a potent oncogenic driver in a wide spectrum of tumors

Isabel Fernández-Pisonero,[1,2,3] Laura Clavaín,[1,2,3] Javier Robles-Valero,[1,2,3] L. Francisco Lorenzo-Martín,[1,2,3] Rubén Caloto,[1,2,3] Blanca Nieto,[1,2] Carmen García-Macías,[1,2] Clara L. Oeste,[4] Manuel Sánchez-Martín,[5] Antonio Abad,[1,2,3] Alejandro Hortal,[4] Dolores Caballero,[1,2,3] Marcos González,[1,2,3] Mercedes Dosil,[1,2,3] Balbino Alarcón,[4] and Xosé R. Bustelo[1,2,3,6,*]

[1]Centro de Investigación del Cáncer, CSIC-Universidad de Salamanca, 37007 Salamanca, Spain
[2]Instituto de Biología Molecular y Celular del Cáncer, CSIC-Universidad de Salamanca, 37007 Salamanca, Spain
[3]Centro de Investigación Biomédica en Red de Cáncer (CIBERONC), CSIC-Universidad de Salamanca, 37007 Salamanca, Spain
[4]Centro de Biología Molecular Severo Ochoa, CSIC-Universidad Autónoma de Madrid, 28049 Madrid, Spain
[5]Nucleus Platform, Universidad de Salamanca, 37007 Salamanca, Spain
[6]Lead contact
*Correspondence: xbustelo@usal.es
https://doi.org/10.1016/j.celrep.2022.110522

SUMMARY

A missense change in *RRAS2* (Gln[72] to Leu), analogous to the Gln[61]-to-Leu mutation of RAS oncoproteins, has been identified as a long-tail hotspot mutation in cancer and Noonan syndrome. However, the relevance of this mutation for *in vivo* tumorigenesis remains understudied. Here we show, using an inducible knockin mouse model, that R-Ras2[Q72L] triggers rapid development of a wide spectrum of tumors when somatically expressed in adult tissues. These tumors show limited overlap with those originated by classical *Ras* oncogenes. R-Ras2[Q72L]-driven tumors can be classified into different subtypes according to therapeutic susceptibility. Importantly, the most relevant R-Ras2[Q72L]-driven tumors are dependent on mTORC1 but independent of phosphatidylinositol 3-kinase-, MEK-, and Ral guanosine diphosphate (GDP) dissociation stimulator. This pharmacological vulnerability is due to the extensive rewiring by R-Ras2[Q72L] of pathways that orthogonally stimulate mTORC1 signaling. These findings demonstrate that *RRAS2[Q72L]* is a *bona fide* oncogenic driver and unveil therapeutic strategies for patients with cancer and Noonan syndrome bearing *RRAS2* mutations.

INTRODUCTION

The recent characterization of cancer genomes has unexpectedly revealed that most driver mutations are found at low and intermediate frequencies across tumor types (ICGC/TCGA Pan-Cancer Analysis of Whole Genomes Consortium, 2020; Garraway and Lander, 2013; Scholl and Fröhling, 2019). This entails several problems for cataloging the key genes involved in cancer. One of them is that we are still far from obtaining the full picture of the driving mutations that are important for tumor development. For example, a recent estimate has calculated that, depending on the average mutational burden of each tumor type, sequencing of a minimum of 650–5,300 independent tumor samples will be required to identify all driver genes present at low frequency in affected individuals (Lawrence et al., 2014). Another problem is defining the exact functional role of the long-tail driver mutations in tumor formation and progression. In this context, the most orthodox model posits that these mutations play roles like those carried out by the cancer genes that are found at higher frequency in tumors. However, other models postulate that some of those mutations could only provide an incremental selective advantage to already transformed cells (Castro-Giner et al., 2015).

R-RAS2 (also known as TC21) is a RAS-like GTPase in which long-tail hotspot mutations (Q72L/H) have been found in pan-cancer studies (Bailey et al., 2018; Chang et al., 2016). This mutated residue is in a position analogous to the Gln[61] found in classical RAS proteins (the shift in numbers is due to the presence of an 11-amino-acid-long N-terminal sequence in the primary structure of R-RAS2). Mutations in that residue are known to block guanosine triphosphate (GTP) hydrolysis in RAS superfamily proteins, generating constitutively active GTPases that are preferentially bound to GTP (Buhrman et al., 2010; Scheidig et al., 1999). Other *RRAS2* mutations analogous to those affecting the Gly[12], Gly[13], and Ala[59] residues of classic RAS proteins have also been detected in tumors. Using more focalized approaches, *RRAS2* mutations have been found at higher frequencies in central nervous system germinomas (14.6% of interrogated cases) and KIT+ germ cell tumors (11.8% of cases) (Mata et al., 2020; Schulte et al., 2016). Underscoring the potential interest for human disease, *RRAS2* mutations have been identified in individuals with Noonan syndrome (Capri et al., 2019; Niihori et al., 2019), a rare developmental disease frequently associated with deregulation of RAS signaling elements (Bustelo et al., 2018; Simanshu et al., 2017).
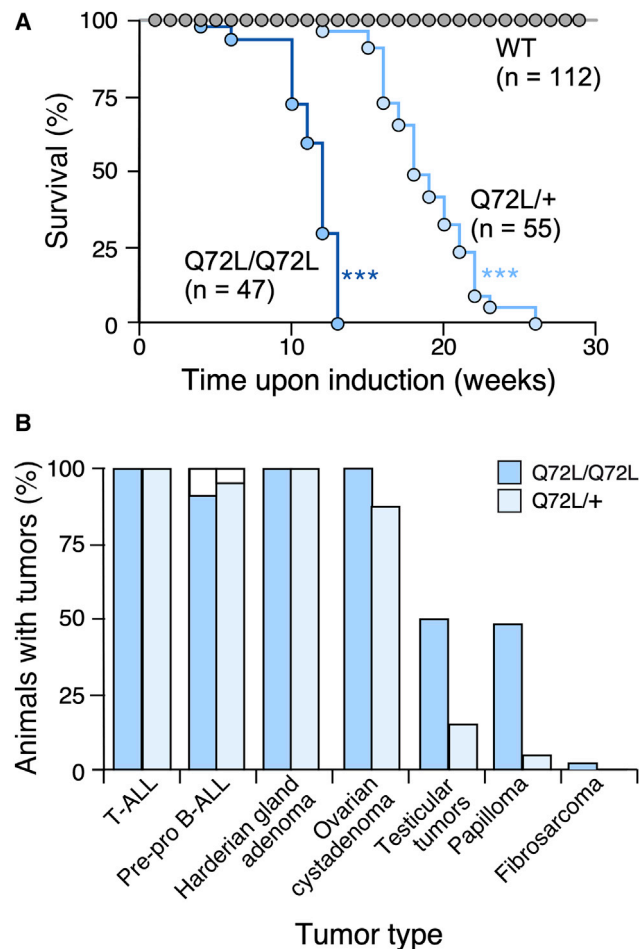
Figure 1. Somatic expression of R-Ras2^{Q72L} promotes tumor formation in mice

(A) Survival curves of tamoxifen-treated mice of the indicated genotypes. The number of mice analyzed is indicated in the figure (the same was done for other figures). Q72L/Q72L, tamoxifen-treated iCre-*Rras2*$^{Q72L/Q72L}$ mice; Q72L/+, tamoxifen-treated iCre-*Rras2*$^{Q72L/+}$ mice. ***p ≤ 0.001 using log rank (Mantel-Cox) test.

(B) Spectrum and penetrance of tumors found in iCre-*Rras2*$^{Q72L/Q72L}$ and iCre-*Rras2*$^{Q72L/+}$ mice 2.5 and 4–5 months after tamoxifen treatment, respectively. The white boxes in the pre-pro-B-ALL columns indicate that, in a low percentage of mice, these tumors could not be identified by histological analyses because of extensive infiltration of the spleen by T-ALL cells.

See also Figure S1.

Given that genetically engineered mouse models for the *RRAS2* hotspot mutation have not been developed up to now, the relevance of this mutation for tumor development and/or progression remains unknown. However, it has been observed, using ectopic expression systems in immortalized cell lines, that R-RAS2^{Q72L} and other gain-of-function (GoF) mutant versions of R-RAS2 show transforming activity (Chan et al., 1994; Graham et al., 1994). Cell-based studies have also revealed a high level of similarity of R-RAS2 to classic RAS proteins, including overlapping subcellular localization and effectors, such as phosphatidylinositol 3-kinase α (PI3Kα), RAF, and Ral guanosine diphosphate (GDP) dissociation stimulator

(RalGDS). In line with this, *RRAS2*-transformed cells usually display high levels of phospho (p)-AKT and p-ERK (Calvo and Crespo, 2009; Cox et al., 1994; Graham et al., 1999; López-Barahona et al., 1996; Movilla et al., 1999; Ohba et al., 2000; Rosario et al., 1999; Zhang et al., 2017). However, contrary to the idea of a fully redundant role of R-RAS2 with classic RAS proteins, it has been shown that ectopic expression of R-RAS2 cannot rescue the proliferative defect caused by elimination of the three Ras proteins in mouse embryonic fibroblasts (Drosten et al., 2010).

Despite these observations, there are no actual data demonstrating that the *RRAS2*^{Q72L} hotspot mutation behaves as a truly oncogenic driver *in vivo* and, if that were the case, the spectrum of tumor types, pathobiological programs, and therapeutic vulnerabilities induced by this mutant protein. To approach these issues, here we investigated the specific role of the endogenous R-RAS2^{Q72L} using an *ad hoc*-designed knockin mouse model.

RESULTS

R-Ras2^{Q72L} promotes tumor formation in mice

To investigate whether endogenous *RRAS2*^{Q72L} acts as an oncogenic driver *in vivo*, we generated a Cre-ER^{T2} (Cre recombinase fused to the mutated ligand-binding domain of the human estrogen receptor)-regulated mouse strain (iCre-*Rras2*^{Q72L}; Figure S1A) that allows swapping of the wild-type (WT) allele by the *Rras2*^{Q72L} mutant one at any desired time in systemic and tissue-specific manners using tamoxifen injections and infections with adenoviral particles encoding the Cre recombinase (hereafter called adeno-Cre), respectively (Figure S1B). We observed that the somatic expression of R-Ras2^{Q72L} leads to rapid death of 100% of animals few weeks after tamoxifen administration (Figure 1A). Necropsies revealed the presence of T cell acute lymphoblastic leukemia (T-ALL; Figure 1B) in the thymus (Figure 2A) and peripheral tissue (Figure S2A), intrasplenic pre-pro-B cell acute lymphoblastic leukemia (pre-pro-B-ALL; Figures 1B and 2B), Harderian gland adenomas (Figures 1B and 2C), *rete ovarii*-derived cystadenomas (Figures 1B and 2D), *rete testis*-derived tumors (Figures 1B and 2E), papillomas concentrated in areas of frequent skin abrasion (Figures 1B and 2F), and high-grade spindle cell mesenchymal tumors that have been classified as fibrosarcomas (Figures 1B and 2G). The death of these animals is a direct consequence of the highly aggressive T-ALL, which impairs breathing and vital organ functions because of enlargement of the thymus (Figure 2A) and development of metastases (Figure S2A), respectively. The transformation of R-Ras2^{Q72L} is dependent on the allelic dose because we observed an ≈2-fold reduction in the average death curves in tamoxifen-treated heterozygous iCre-*Rras2*$^{Q72L/+}$ animals (Figure 1A). However, mice heterozygous and homozygous for the mutant *Rras2* allele show comparable spectra and incidence of tumors (Figure 1B).

Further *de visu* analyses revealed masses of mesenchymal cells scattered in the serosa of most abdominal organs (Figure S2B), adipose tissue (Figure S2C), and skin (Figure S2D) in all tamoxifen-treated animals analyzed (n = 47). These masses, which show different degrees of hyperplastic progression (Figures S2C–S2E), are likely precursors of the mesenchymal tumors
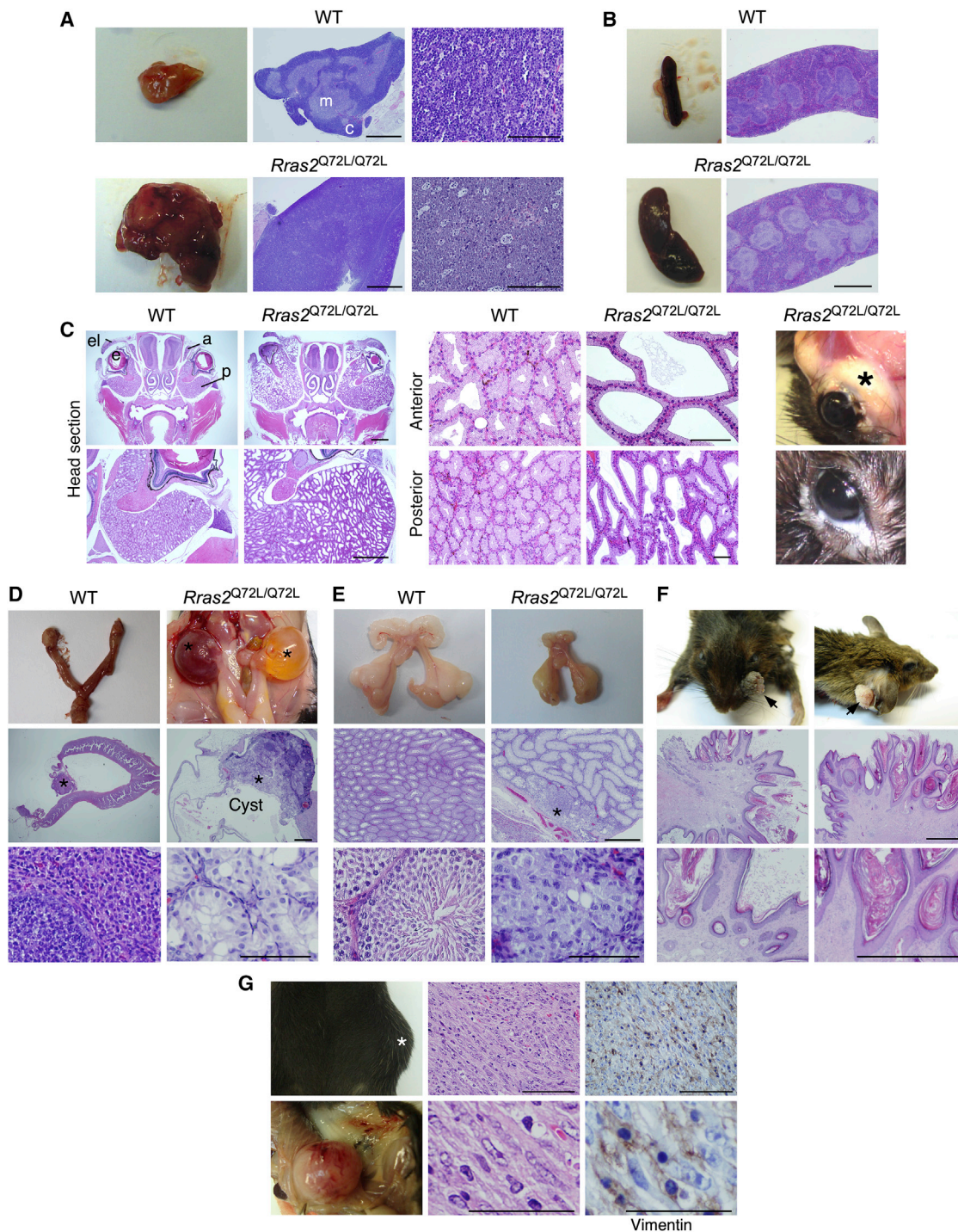
Figure 2. Examples of tumors formed upon somatic expression of R-Ras2^{Q72L}

(A) Images of thymi (left panels) and hematoxylin-and-eosin-stained thymus sections (center and right panels) from mice of the indicated genotypes at the endpoint of the experiment shown in Figure 1A. c, cortex; m, medulla. Scale bars, 1 mm (center panels) and 100 μm (right panels).

(B) Images of a spleen (left) and hematoxylin-and-eosin-stained spleen sections from mice of the indicated genotypes at the endpoint of the experiment shown in Figure 1A. Scale bar, 1 mm.

(C) Left and center panels: hematoxylin-and-eosin-stained section of Harderian glands from mice of the indicated genotypes at the endpoint of the experiment shown in Figure 1A. a, anterior gland; p, posterior gland; e, eye; el, eyelid. Scale bars, 1 mm (left panels) and 100 μm (center panels). Right panels: images of Harderian glands (top, asterisk) and milky exudates (bottom) found in the eyes of tamoxifen-treated iCre-*Rras2*$^{Q72L/Q72L}$ mice.

(legend continued on next page)

found in some of these animals (Figures 1B and 2G). We also detected recurrent endometrial glandular hyperplasias in tamoxifen-treated female iCre-Rras2$^{Q72L/Q72L}$ mice (Figure S2F).

To rule out the possibility that some tumor types do not develop at significant frequencies because of the very short lifespan of R-Ras2^{Q72L}-expressing animals (Figure 1A), we induced the mutant protein in endometrial and mesenchymal cells using the tissue-specific adeno-Cre delivery approach (Figure S1B). We also included the lungs and bladder in these experiments because some oncogenic RRAS2 mutations are found at low frequencies in tumors from those tissues, according to pan-cancer data. In the case of uteri, we found further progression of the pathology seen in the tamoxifen-treated iCre-Rras2^{Q72L} mice (Figure S2F) toward more advanced cystic endometrial hyperplasia (Figures S2G and S2H). However, no tumors were formed under these conditions in the endometrium, lungs, or bladder, even 9 months after the recombination step (Figure S2G). Subcutaneous or intraperitoneal injections of adeno-Cre particles promote fibrosarcoma in 40%–50% of the animals tested between 4 and 5 months after expression of R-Ras2^{Q72L} (Figures S2G and S2I). These results qualify the hotspot Q72L mutation of RRAS2 as a bona fide oncogenic driver.

Rras2^{Q72L}-driven tumors show tissue-specific pharmacological vulnerabilities

Given the implication of RRAS2 in activation of the PI3Kα, ERK, and RalGDS pathways (Graham et al., 1994; López-Barahona et al., 1996; Movilla et al., 1999; Rosario et al., 2001), we next carried out pharmacological and genetic experiments to identify the downstream elements that are critical for the fitness of R-Ras2^{Q72L}-driven tumors. We first treated cohorts of 4-week-old iCre-Rras2$^{Q72L/Q72L}$ mice with tamoxifen to induce tumor formation, and 4 weeks later, we subjected them to chronic treatments with the inhibitors ETP-46321 (specific for PI3Kα and PI3Kδ), ETP-992 (targeting all PI3K isoforms and mTORC1), rapamycin (specific for mTORC1), and PD0325901 (specific for MEK) (Figure 3A). We found that only rapamycin and ETP-992, both of which target mTORC1, prevent death of the tamoxifen-treated iCre-Rras2$^{Q72L/Q72L}$ animals (Figure 3B). This protection is probably due to elimination of the lethal T-ALL that develops in these mice (Figures 3C and 3D). Necropsy of these animals revealed three main subtypes of Rras2^{Q72L}-driven cancers according to drug susceptibility (Figure 3D): (1) PI3Kα/δ- and mTORC1-dependent but MEK1/2-independent tumors (ovarian cystadenomas), (2) mTORC1-dependent but PI3Kα/δ- and MEK1/2-in-

dependent tumors (T-ALL, pre-pro B-ALLs, the mesenchymal hyperplasia condition), and (3) tumors resistant to all the inhibitors tested (testicular tumors, Harderian gland adenomas, and papilloma).

Given the lack of inhibitors, we generated an iCre-Rras2$^{Q72L/Q72L}$;Ralgds$^{-/-}$ strain to assess the importance of RalGDS in R-Ras2^{Q72L}-driven tumorigenesis. Genetic ablation of RalGDS does not change the latency and type of most tumors found in single tamoxifen-treated iCre-Rras2$^{Q72L/Q72L}$ mice (Figures 3E–3G). Fibrosarcoma is the only exception because its incidence rises 11-fold in iCre-Rras2$^{Q72L/Q72L}$;Ralgds$^{-/-}$ mice (Figure 3F). This increased tumorigenicity correlates with detection of more accentuated mesenchymal hyperplasias in the serosa and dermis of these mice (Figure 3H). These findings indicate that R-Ras2^{Q72L}-driven tumors are highly diverse in terms of dependency on the activity of the main downstream effector molecules. However, the mTORC1 pathway seems to be the most important Achilles' heel in the case of the most prevalent subclasses of Rras2^{Q72L}-driven tumors. Our results also indicate that that PI3Kα, MEK, and RalGDS play marginal roles per se in the fitness of most Rras2^{Q72L}-driven tumors.

R-Ras2^{Q72L}-driven T-ALLs are Notch1 dependent

To dissect the signaling pathways involved in R-Ras2^{Q72L}-driven tumorigenesis, we next characterized the biological and signaling features of T-ALL and fibrosarcoma cells obtained from iCre-Rras2$^{Q72L/Q72L}$ mice. In the case of T-ALL, Rras2^{Q72L}-driven leukemias can be ascribed to four groups according to surface immunophenotype criteria: CD4$^-$ CD8$^-$ (double negative [DN]), CD4$^+$ CD8$^+$ (double positive [DP]), single CD4$^+$, and single CD8$^+$ cells (Figures S3A and S3B). Frequently, these tumors show a mixture of those subclasses (Figures S3A–S3G). DN T-ALL cells exhibit surface immunophenotypic features typically found in immature DN3b thymocytes (CD44$^-$, CD25$^+$, positive for the intracellular β subunit of the T cell receptor [icTCRβ$^+$] and negative for membrane-localized TCRβ [mTCRβ$^-$]) (Figures S3C and S3D). DP T-ALLs are CD24$^+$, icTCRβ$^+$, and mTCRβ$^-$, features that do not correspond to any normal developmental stage (Figures S3B, S3C, and S3E). Likewise, 100% of CD4$^+$ and 71.4% of CD8$^+$ T-ALLs cannot be assigned to a defined maturation state of normal lymphocytes (Figure S3C), given that they are icTCRβ$^+$ but mTCRβ$^-$ and CD24$^+$ (Figures S3F and S3G). However, it is likely that these T-ALLs represent transformed populations of mature T cells that have

(D) Top panels: images of the female reproductive system from mice of the indicated genotypes at the endpoint of the experiment shown in Figure 1A. Tamoxifen-treated iCre-Rras2^{Q72L} mice develop serous cysts (top right panel, asterisks) that, in some cases, become hemorrhagic. Center panels: histology of a normal ovary and uterus (left) and an incipient tumor (right, asterisk) found in R-Ras2^{Q72L}-expressing mice. Scale bars, 1 mm. Bottom panels: enlarged images of the histologies shown in the center panels. As a control, we included a normal ovary section (left). Scale bars, 100 μm.
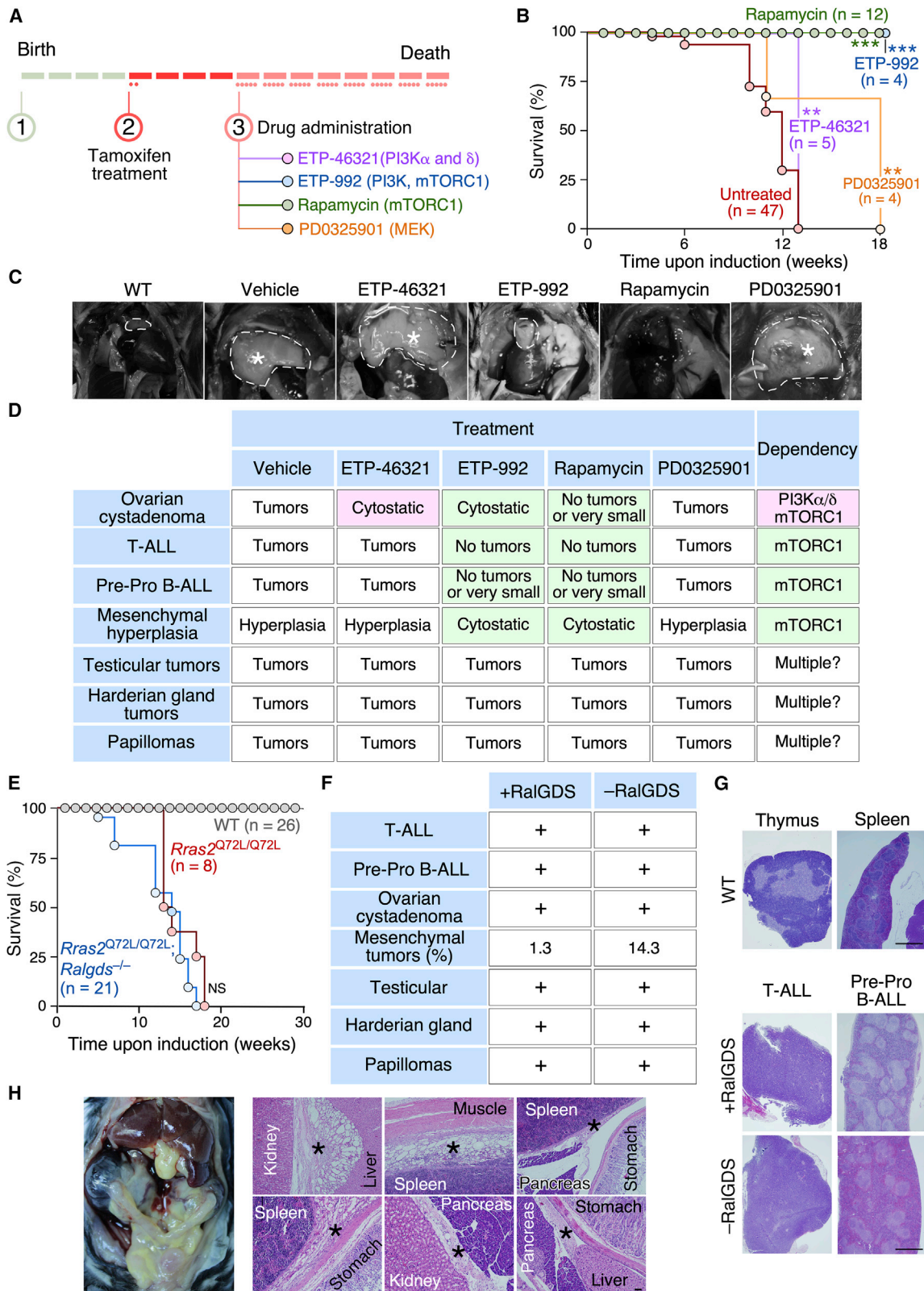
(E) Top panels: images of the male reproductive system from mice of the indicated genotypes at the endpoint of the experiment shown in Figure 1A. Center panels: histology of a normal testis (left) and of an incipient tumor formed from rete testis cells (right). Bottom panels: enlarged images of the histologies shown in the center panels. Scale bars, 1 mm (center panels) and 100 μm (bottom panels).

(F) Top panels: images of the papillomas formed in tamoxifen-treated iCre-Rras2^{Q72L} mice at the end of the experiment shown in Figure 1A. Bottom panels: examples of the histology of the papillomas found in those animals. Scale bars, 1 mm (center panels) and 100 μm (bottom panels).

(G) Left panels: image of a tumor (asterisk) found in adeno-Cre-treated iCre-Rras2^{Q72L} mice that was identified as a high-grade mesenchymal tumor according to pathological analyses. Center panels: histology of the tumor shown in the left panel. Right panels: staining of a tumor section with antibodies to vimentin. Scale bars, 100 μm (top panels) and 50 μm (bottom panels).

See also Figure S2.

A

B

C

WT | Vehicle | ETP-46321 | ETP-992 | Rapamycin | PD0325901

D

	Treatment					Dependency
	Vehicle	ETP-46321	ETP-992	Rapamycin	PD0325901	
Ovarian cystadenoma	Tumors	Cytostatic	Cytostatic	No tumors or very small	Tumors	PI3Kα/δ mTORC1
T-ALL	Tumors	Tumors	No tumors	No tumors	Tumors	mTORC1
Pre-Pro B-ALL	Tumors	Tumors	No tumors or very small	No tumors or very small	Tumors	mTORC1
Mesenchymal hyperplasia	Hyperplasia	Hyperplasia	Cytostatic	Cytostatic	Hyperplasia	mTORC1
Testicular tumors	Tumors	Tumors	Tumors	Tumors	Tumors	Multiple?
Harderian gland tumors	Tumors	Tumors	Tumors	Tumors	Tumors	Multiple?
Papillomas	Tumors	Tumors	Tumors	Tumors	Tumors	Multiple?

E

F

	+RalGDS	−RalGDS
T-ALL	+	+
Pre-Pro B-ALL	+	+
Ovarian cystadenoma	+	+
Mesenchymal tumors (%)	1.3	14.3
Testicular	+	+
Harderian gland	+	+
Papillomas	+	+

G

Thymus | Spleen
WT
T-ALL | Pre-Pro B-ALL
+RalGDS
−RalGDS

H

lost membrane expression of the TCR (Figure S3C). This defect, which is also common to DP T-ALLs, could represent an exacerbation of the role of endogenous R-Ras2^{WT} in TCR recycling (Martinez-Martin et al., 2011). Finally, a smaller percentage (28.5%) of CD8$^+$ T-ALLs display features of activated mature T cells according to mTCRβ$^+$ and CD24$^+$ status (Figures S3G and S3C). T-ALL cells from these mice can regenerate highly disseminated tumors when introduced into WT recipient mice (Figures S3H–S3J), confirming their transformed status. This leukemogenic process is also T cell autonomous because T-ALLs can be generated when R-Ras2^{Q72L} is specifically expressed in immature thymocytes (Figure S3K).

Flow cytometry experiments revealed that R-Ras2^{Q72L}-driven T-ALLs display high levels of p-AKT upon isolation from the thymus (Figure 4A). However, such levels cannot be maintained in the long term unless the T-ALL cells lose the tumor suppressor *Pten* (see below; Figure 4F). Unlike in the case of p-AKT, these cells exhibit WT-like levels of p-ERK (Figure 4A). We also found that T-ALL cells display high levels of the active, intracellular domain of Notch1 (ICN1) (Figure 4B). In agreement with these data, these cells show upregulation of ICN1 target genes such as *Notch1*, *Hes1*, *Myc*, and *Cdkn2a* (Figure 4C). They also rely on active Notch1 signaling because they need bone marrow stromal cells expressing the Notch1 ligand Delta1 to be maintained in cell culture (I.F.-P. and X.R.B., unpublished data). In line with this, the growth and long-term viability of the cultured cells is impaired by addition of Notch1 inhibitors (Figure 4D).

We observed that all primary leukemic cells from iCre-*Rras2*$^{Q72L/Q72L}$ mice retain expression of PTEN (Figure 4E), a tumor suppressor phosphatase that is frequently lost in Notch1-driven T-ALLs (Gutierrez et al., 2009; Silva et al., 2008; Van Vlierberghe and Ferrando, 2012). Most T-ALL isolates (64.3%, n = 14) retain PTEN$^+$ status even after long-term co-culture with Delta1-expressing stromal cells (Figures 4E and 4F), a feature not usually observed in other experimental T-ALL models (Silva et al., 2008). Elimination of PTEN usually correlates with a reduction in the electrophoretic mobility of ICN1 (Figures 4E and 4F) and a strong elevation in p-AKT levels (Figure 4F). In line with the data obtained in mice, we found that R-Ras2^{Q72L} T-ALL cells are sensitive to mTORC1 but not to PI3K inhibitors irrespective of their PTEN status (Figure 4G).

Given that the above results suggested a synergism between the R-Ras2^{Q72L} and Notch1 pathways in T cell leukemogenesis, we next carried out bone marrow transplantation experiments to analyze the leukemogenic activity of ICN1 depending on the

mutational status of the endogenous *Rras2* gene. We purified bone marrow precursor (BMP) cells from control and tamoxifen-treated iCre-*Rras2*$^{Q72L/Q72L}$ mice and, after transducing them with retroviruses bicistronically encoding ICN1 and GFP, transplanted them into lethally irradiated WT recipient mice (Figure S3L). As a comparative control, we used *Rras2*$^{Q72L/Q72L}$ BMP cells (Figure S3L). As expected (Li et al., 2008), ICN1-transduced WT BMP cells can rapidly form T-ALLs (t$_{1/2}$ = 7 weeks after implantation) (Figure 4H). *Rras2*$^{Q72L/Q72L}$ BMP cells also induce T-ALL upon transplantation in mice, although with larger latencies than ICN1+GFP-transduced WT BMP cells (Figure 4H). Leukemogenesis is accelerated significantly when ICN1 is expressed in *Rras2*$^{Q72L/Q72L}$ BMP cells (t$_{1/2}$ = 4 weeks after implantation) (Figure 4H). These data indicate that R-Ras2^{Q72L} and ICN1 cooperate in the transformation of BMP cells. Further highlighting the interconnection of ICN1 and R-Ras2 signaling, the transforming activity of ICN1 is abrogated when transduced into *Rras2*$^{-/-}$ BMPs (Figure S3L and 4H). These data demonstrate that R-Ras2^{Q72L} and ICN1 interact synergistically in T cell acute lymphoblastic leukemogenesis. They also indicate that R-Ras2^{Q72L}- and Notch1-driven T-ALL are Notch1 and R-Ras2^{WT} dependent, respectively.

Endogenous R-Ras2^{Q72L} is essential for *Rras2*^{Q72L}-transformed mesenchymal cells

In the case of fibrosarcoma, we isolated five tumor cell lines from iCre-*Rras2*$^{Q72L/Q72L}$ mice (fibrosarcoma [FS]#2–FS#5). These tumor cells exhibit a spindle-shaped phenotype that is reminiscent of that found in NIH 3T3 cells transformed by ectopically expressed R-RAS2^{Q72L} (Figure 5A). They can also form tumors when implanted subcutaneously in WT mice (Figure 5B), confirming that they have acquired a transformed condition. Gene editing experiments indicated that ablation of endogenous R-Ras2^{Q72L} is probably lethal for these FS cells because we could only generate FS#2 cell lines heterozygous for the *Rras2* null allele (Figure 5C). Given these results, we explored the possibility that use of *Rras2*-specific short hairpin RNAs (shRNAs) could facilitate generation of FS#2 cells expressing minimal levels of endogenous R-Ras2^{Q72L} that could be compatible with some residual proliferative activity. In line with this hypothesis, we could generate several FS#2 knockdown clones showing a strong (sh#89 and sh#478) or mild (sh#751 and sh#752) reduction in the levels of oncogenic R-Ras2 (Figure 5D). Analysis of these cell clones indicated that expression

---

Figure 3. *Rras2*^{Q72L}-driven tumors show tissue-specific pharmacological vulnerabilities

(A) Schematic of experiments. Each interval shown on the top line represents a week in the life of the animals. Single dots indicate the time of administration of tamoxifen (red dots) or of the indicated drugs (light red dots).

(B) Survival curves of the indicated cohorts of mice. **p ≤ 0.01, ***p ≤ 0.001 using log rank (Mantel-Cox) test.

(C) Images of the thymus (areas inside dashed lines) at the end of the experiments shown in (B). Asterisks indicate enlarged thymi because of the T-ALL condition.

(D) Effects of the indicated inhibitors (top) on the pathologies (left) developed in tamoxifen-treated iCre-*Rras2*$^{Q72L/Q72L}$ mice. Tumors that are PI3K and mTORC1 dependent are highlighted in a purple and green background, respectively. Tumors that are not affected by any of the inhibitors used are shown in open boxes.

(E) Survival curves of tamoxifen-treated mice of the indicated genotypes. NS, not statistically significant according to the log rank (Mantel-Cox) test applied.

(F) Effect of RalGDS deficiency on R-Ras2^{Q72L}-driven tumors and pathologies according to data obtained in (E).

(G) Histology of a normal thymus and spleen (top) and of the R-Ras2^{Q72L}-driven T-ALL and pre-pro-B-ALL found in the presence and absence of RalGDS (bottom panels). Scale bar, 1 mm.

(H) Left panel: representative image of the abdomen of an iCre-*Rras2*$^{Q72L/Q72L}$;*Ralgds*$^{-/-}$ mouse 2.5 months after tamoxifen treatment. Right panels: example of a mesenchymal hyperplasia (black asterisks) found in iCre-*Rras2*$^{Q72L/Q72L}$;*Ralgds*$^{-/-}$ mice 2.5 months after tamoxifen injections. Scale bar, 100 μm.
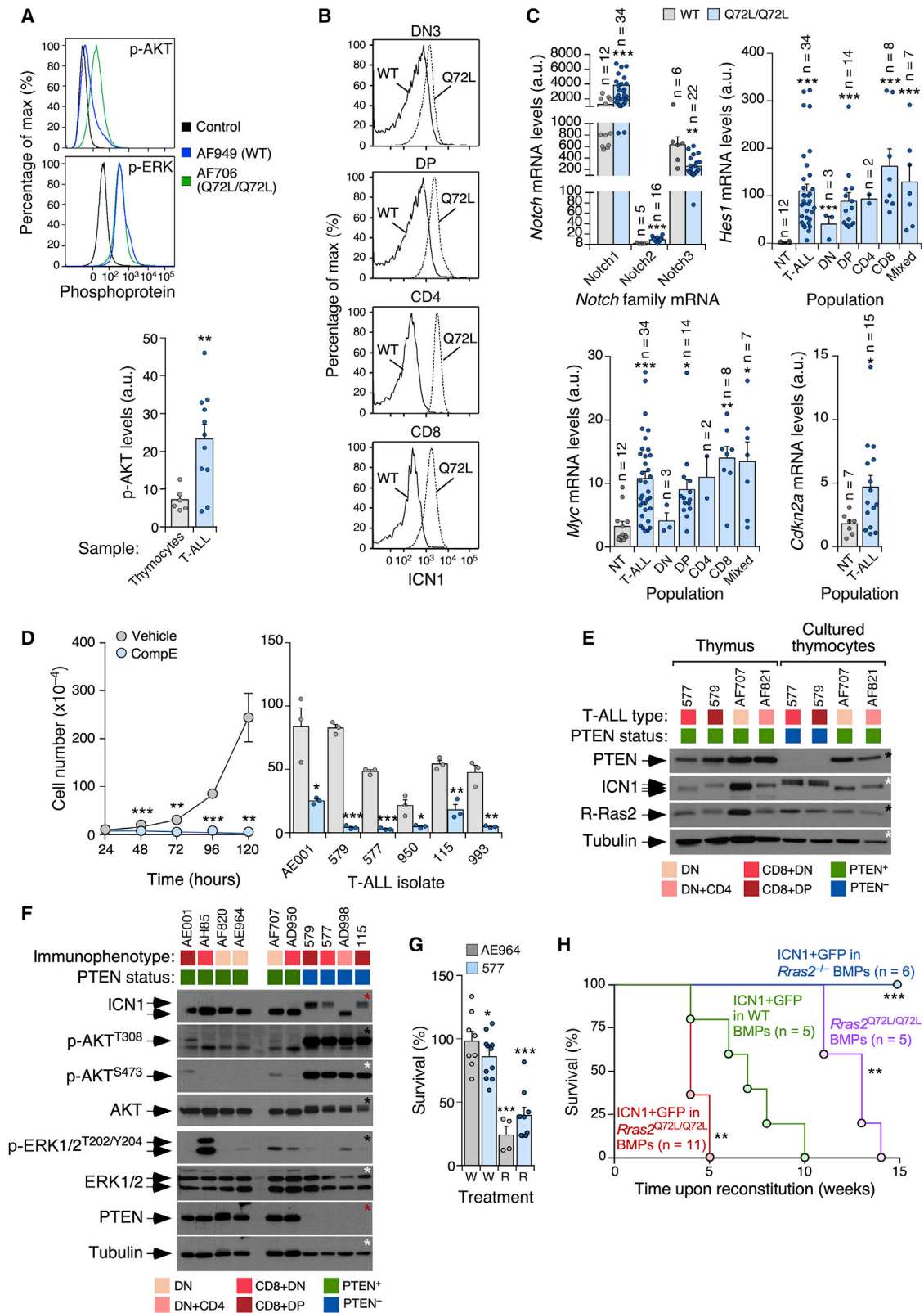
of R-Ras2^Q72L directly correlates with the proliferation rates shown by the knockdown cells (Figure 5D). These cells eventually regain control-like levels of R-Ras2^Q72L (Figure 5E, top panel) and normal proliferation rates (Figure 5E) upon a few passages in culture, indicating that R-Ras2^Q72L is essential for the transformation and maintenance of the transformed state of mouse fibroblasts.

We used two of the best *Rras2*^Q72L knockdown FS#2 cells (sh#478 and sh#89) at low passages to investigate the effect of R-Ras2 depletion on downstream signaling. As a control, we used an FS#2 derivative expressing a scrambled shRNA (pLKO). The two knockdown cells displayed a slight reduction in p-AKT levels compared with controls (Figure 5F). In contrast, no major changes in p-ERK1/2 are detected among the examined cells (Figure 5F). It is likely that this mild signaling defect is due to activation of compensatory mechanisms (see below). Despite this, we found that depletion of R-Ras2^Q72L is associated with a more significant reduction in the phosphorylation levels of the downstream mTORC1 elements p70S6K and S6RP (Figure 5F).

To further assess the effects of depletion of R-Ras2^Q72L on FS cells, we carried out genome-wide gene expression analyses between control cells and one of the *Rras2*^Q72L knockdown FS (sh#89) cell lines (Figure S4A; Table S1). Confirming our pathological analyses (Figures 1B, 2G, S2B–S2E, and S2I), we found, using *in silico* analyses, that the transcriptome of the control FS#2 cell line is more FS- than leiomyosarcoma-like (Figure S4B). Gene set enrichment analyses (GSEAs) revealed the presence of gene signatures associated with mTORC1 signaling (Figure 5G), Myc and E2F transcriptional activity, oxidative phosphorylation, DNA damage, and Hedgehog signaling in the downregulated transcriptome of *Rras2*^Q72L knockdown cells (Figures S4D and S4E). All of these molecular features have been linked previously to mTORC1 signaling (Csibi et al., 2014; Larsen and Møller, 2020; Michaloglou et al., 2018; Wu et al., 2017; Yuan

et al., 2018). In contrast, the upregulated transcriptome of *Rras2*^Q72L knockdown cells is enriched in gene programs commonly associated with myofibroblasts (Figure 5G). This subset includes gene signatures related to myogenic processes, transforming growth factor β (TGF-β) signaling, epithelial-mesenchymal transition (EMT), and cytoskeletal processes (Figures S4D and S4F; Hinz, 2007; Hu and Phan, 2013). Concurring with these data, we found, using immunofluorescence studies, that the *Rras2*^Q72L knockdown promotes an increase in the number of cells exhibiting filaments of α-smooth muscle cell actin (Figures 5H and S4G). This feature is typically seen in differentiated myofibroblasts (Hinz, 2007; Hu and Phan, 2013; Tomasek et al., 2002). We also found that *Rras2*^Q72L knockdown cells display larger areas (Figure S4H) and a more rounded morphology (Figure S4I) than controls. A similar cellular phenotype has been observed previously in rat renal fibroblasts upon treatment with mTORC1 inhibitors (Winbanks et al., 2007), implying that the quiescent myofibroblast state found in R-Ras2^Q72L-depleted cells is due to downregulation of the mTORC1 pathway. Finally, we found that the upregulated transcriptome of *Rras2*^Q72L knockdown cells contains a large set of tyrosine kinase ligands and cytokines that could explain the mild defects in p-AKT and p-ERK levels seen in knockdown cells (Figure S4C; Table S1). Interestingly, the gene expression subset that becomes downregulated in sh#89 FS#2 cells is the one showing more similarity with the transcriptome of FS cases (Figure S4J). Such a similarity is not observed in the case of the upregulated gene subset (Figure S4J). These results indicate that the *Rras2*^Q72L knockdown is associated with reduced levels of expression of genes involved in mTORC1-dependent proliferative and metabolic programs, generation of a quiescent myofibroblast state, and stimulation of a variety of autocrine loops mediated by cytokines and mitogenic factors (Figure S4K).

Given that the autocrine loops described above could obscure the signaling defects of *Rras2*^Q72L knockdown cells, we decided

Figure 4. R-Ras2^Q72L-driven T-ALLs are Notch1 dependent

(A) Example (top panels) and quantification (bottom graph) of p-AKT and p-ERK levels found in cells freshly isolated from the thymi of control (WT) and tamoxifen-treated iCre-*Rras2*^Q72L/Q72L (Q72L/Q72L) mice. In the top panels, "control" indicates values obtained with cells incubated with the negative control antibody. In the graph, dots represent values from individual samples. Bars represent the mean ± SEM. **p < 0.01 using two-tailed Student's t test.

(B) ICN1 expression levels in the indicated subpopulations of R-Ras2^Q72L-driven T-ALL cells.

(C) Expression of transcripts for *Notch* family members (top left panel) and ICN1 target genes (all other panels) in non-fractionated and/or fractionated thymocyte subpopulations from mice of the indicated genotypes (inset). NT, normal thymocytes from WT mice; T-ALL, unfractionated T-ALL cells; DN, double-negative (CD4⁻ CD8⁻) T-ALL; DP, double-positive (CD4⁺CD8⁺) T-ALL; CD8, single-positive CD8 T-ALL cells, CD4, single-positive CD4 T-ALL cells; Mixed, T-ALL cells displaying a combination of the foregoing surface immunophenotypes. Bars represent the mean ± SEM relative to WT controls.*p ≤ 0.05, **p ≤ 0.01, ***p ≤ 0.001 using two-tailed Student's t tests (top left and bottom right panels) or one-way ANOVA and Dunnett's multiple comparison test (top right and bottom left panels).

(D) Left panel: growth curve of freshly isolated T-ALL cells (isolate #579) in the presence or absence of compound E (CompE). Values are represented as the mean ± SEM relative to untreated cells. *p ≤ 0.05, **p ≤ 0.01, ***p ≤ 0.001 according to two-tailed Student's t tests (n = 3 technical replicates). Right panel: growth of the indicated T-ALL cell isolates (bottom) cultured in the presence or absence of CompE for 96 h. Bars represent the mean ± SEM relative to untreated cells. *p ≤ 0.05, **p ≤ 0.01, ***p ≤ 0.001 according to two-tailed Student's t tests (n = 3 technical replicates).

(E) Expression of the indicated proteins (left) in T-ALL isolates (top) upon isolation from the thymus (left) and after long-term culture in the presence of OP9-DL1 cells (right). The surface immunophenotype of each clone is indicated at the bottom. The western blot signals obtained using the same filters are indicated by asterisks of the same color. Aliquots of the same cell extracts were always used in independent filters (the same labeling is used in the rest of figures).

(F) Expression of the indicated phosphorylated and total proteins in T-ALL clones shown at the top. The surface immunophenotype and PTEN status of each clone is shown following the color codes indicated at the bottom.

(G) Effect of wortmannin (W) and rapamycin (R) on the viability of indicated PTEN⁺ (AE964) and PTEN⁻ (577) T-ALL cells. Bars represent the mean ± SEM relative to untreated cells (which was given an arbitrary number of 100). *p ≤ 0.05, ***p ≤ 0.001 using ANOVA and Dunnett's multiple comparison tests.

(H) Survival curves of immunocompromised mice injected with the indicated subsets of bone marrow precursor (BMP) cells. **p ≤ 0.01, ***p ≤ 0.001 relative to values obtained in mice transplanted with ICN1+GFP-expressing WT BMP cells according to log rank (Mantel-Cox) test. Sample size is indicated in the panel. See also Figure S3.

Staining with antibodies to α-smooth muscle actin
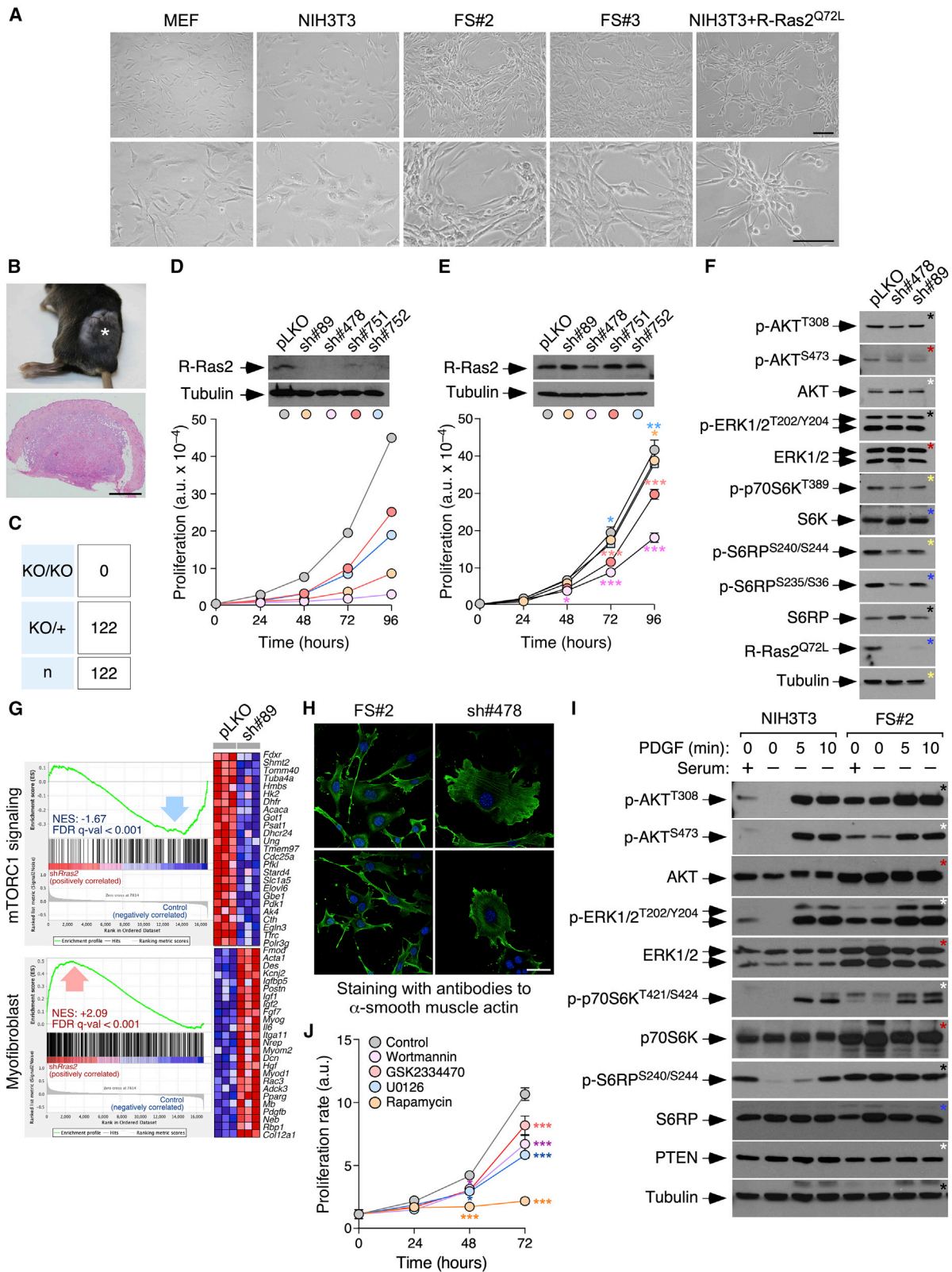
(legend on next page)

to compare the phosphorylation status of AKT, mTORC downstream elements, and ERK in FS#2 and NIH 3T3 cells to get a more direct idea of the signaling alterations elicited by R-Ras2^{Q72L}. These analyses indicated that FS#2 cells do show higher levels of p-AKT, p-ERK1/2, p-p70S6K, and p-S6RP than NIH 3T3 cells under standard and serum starvation conditions (Figure 5I). The phosphorylation levels of all of these proteins are increased upon stimulation of serum-deprived FS cells with platelet-derived growth factor (PDGF) (Figure 5I). Despite activation of these pathways, we observed that proliferation of FS#2 cells is mTORC1 dependent but PI3K, PDK1, and MEK independent (Figure 5J). This dependency is similar to that found in the mesenchymal hyperplasias in R-Ras2^{Q72L}-expressing mice (see above; Figure 3D).

### R-Ras2^{Q72L} promotes cell-type-specific rewiring of the mTORC1 pathway

The drug responses found in these experiments suggest that R-Ras2^{Q72L} promotes mTORC1 activation in a PI3K-independent manner in T-ALL and FS cells (Figures 3D, 4G, and 5J). To shed light on this phenotype, we investigated the effect of inhibitors of the PI3K-AKT and MEK-ERK pathways in the signaling output of R-Ras2^{Q72L}-transformed fibroblasts and T-ALL cells. In the former case, we observed that R-Ras2^{Q72L} promotes phosphorylation of ERK and the PDK1-dependent AKT phosphosite (T^{308}) using the canonical pathways (Figure 6A, left panel). Consistent with this, phosphorylation of AKT and ERK can be blocked by wortmannin and U0126, respectively, in FS#2 and NIH 3T3 cells (Figures 6B and S5A). In contrast, we found that elimination of the mTORC2-dependent AKT phosphosite (S^{473}) requires the combination of PI3K and PDK1 inhibitors in FS#2 cells (Figures 6B and S5A). This suggests that phosphorylation of this site involves convergent signaling inputs from the canonical PI3K-PDK1 pathway (Figure 6A, right panel, pathway a) and a *de novo* PDK1 pathway whose activity is PI3K independent (Figure 6A, right panel, pathway c). Likewise, total elimination of phosphorylation of p70S6K in FS#2 cells requires combinations of PI3K+PDK1 (Figures 6B and S5A), PDK1+MEK (Figures 6B and S5A), or PDK1+RSK1 (ribosomal S6 kinase 1) (Figures 6C and S5B) inhibitors. This suggests that this phosphorylation step is coordinately mediated by

(1) the canonical PI3K-dependent PDK1 pool (Figure 6A, right panel, pathway a) and (2) a PI3K-independent PDK1 pool that feeds signals into the mTORC1 complex in an RSK-independent (Figure 6A, right panel, pathways a and c) and -dependent (Figure 6A, right panel, pathways c and b) manner. Phosphorylation of S6RP follows a similar but not identical regulation as that found in the case of p70S6K. We observed that a single treatment with PI3K and PDK1 inhibitors induces milder changes in the phosphorylation levels of S6RP than p70S6K in FS#2 cells (Figures 6B and S5A, compare the center panels). This suggests that phosphorylation of S6RP must receive extra R-Ras2^{Q72L}-dependent inputs in addition to those derived from p70S6K (Figure 6A, right panel). We also found that, in addition to the combination of inhibitors that block phosphorylation of p70S6K (Figures 6B and S5A), phosphorylation of S6RP can be eliminated by combination of PI3K+MEK inhibitors (Figures 6A, right panel, pathways a and b, 6B, and S5A). Phosphorylation of p70S6K and S6RP can be effectively blocked using just mTORC1 inhibitors (Figures 6D and S5C), indicating that the R-Ras2^{Q72L}-specific input on S6RP phosphorylation must take place downstream of the mTORC1–p70S6K axis (Figure 6A, right panel).

In the case of T-ALL cells, we first focused on the PTEN$^+$ subtype, given that it more accurately mimics the genotypic features found in T-ALL cells isolated from iCre-*Rras2*^{Q72L} mice (see above; Figure 4E). Consistent with the results reported in Figure 4F, PTEN$^+$ T-ALL (AE964) cells exhibit lower levels of p-AKT and p-p70S6K than the PTEN$^-$ T-ALL counterparts (Figure 6E). This is probably due to activation of negative feedback mechanisms like those found previously in cells bearing GoF *PIK3CA* mutations (Vasudevan et al., 2009). In contrast, they keep high levels of p-S6RP (≈40% of those found in the PTEN$^-$ counterparts; Figure 6E, compare the two left lanes in the right panel). This indicates that, as in the case of FS#2 cells, optimal phosphorylation of S6RP involves signaling inputs in addition to those provided by the canonical mTORC1-p70S6K axis (Figure 6A, left panel). Further experiments indicated that p-p70S6K levels can be effectively inhibited by a single administration of PI3K, PDK1, and mTORC1 inhibitors (Figure 6E, left panel; see Figure S6A for the combined results obtained with PTEN$^+$ AE964, AE001,

---

Figure 5. R-Ras2^{Q72L} is essential for the growth of R-Ras2^{Q72L}-transformed mesenchymal cells

(A) Representative images of the indicated cell lines. MEF, mouse embryonic fibroblast; FS, fibrosarcoma. Scale bar, 100 μm.

(B) Example of an FS formed upon subcutaneous injection of FS#2 cells in a recipient mouse (top, asterisk). The histology of the tumor is shown at the bottom. Scale bar, 1 mm.

(C) Quantifications of the FS#2 cell clones homozygous (knockout [KO]/KO) and heterozygous (KO/+) for a null *Rras2*^{Q72L} allele generated after the gene-editing step.

(D) R-Ras2^{Q72L} expression levels and proliferative activity in FS#2 cells expressing a control lentiviral vector (pLKO) or the indicated *Rras2* shRNAs (sh; top). Only a single experiment could be conducted in triplicate in this case because of the difficulty of maintaining the cells with the lowest level of R-Ras2^{Q72L} expression.

(E) R-Ras2^{Q72L} expression levels and proliferative activity of FS#2 cells expressing a control lentiviral vector (pLKO) or the indicated *Rras2* shRNAs after 2 passages in culture. Data are mean ± SEM. *p ≤ 0.05, **p ≤ 0.01, ***p ≤ 0.001 using ANOVA and Dunnett's multiple comparisons tests.

(D and E) n = 3 technical replicates (D) and 3 independent experiments (E).

(F) Phosphorylation and protein expression levels of the indicated proteins (left) on the FS#2 cells shown at the top. The cell nomenclature is the same as in (D).

(G) Downregulation (top) and upregulation (bottom) of the indicated gene signatures (left) in the transcriptome of *Rras2*^{Q72L} knockdown FS#2 cells (sh#89). The false discovery rate (FDR) q value and NES (normalized enrichment score) are indicated in each plot.

(H) Morphological phenotype and intracellular distribution of α-smooth muscle actin (green) in the indicated cells (top). Scale bar, 50 μm.

(I) Phosphorylation and expression levels of the indicated proteins (left) in NIH 3T3 and FS#2 cells maintained under the indicated culture conditions (top).

(J) Proliferation of the FS#2 cell line in the presence of the indicated inhibitors. Concentrations used were 10 nM (rapamycin), 200 nM (wortmannin), 1 μM (GSK2334470), and 20 μM (U0126). Data are mean ± SEM. *p < 0.05, ***p < 0.001 using two-way ANOVA and Dunnett's multiple comparison test (n = 3).

See also Figure S4 and Table S1.
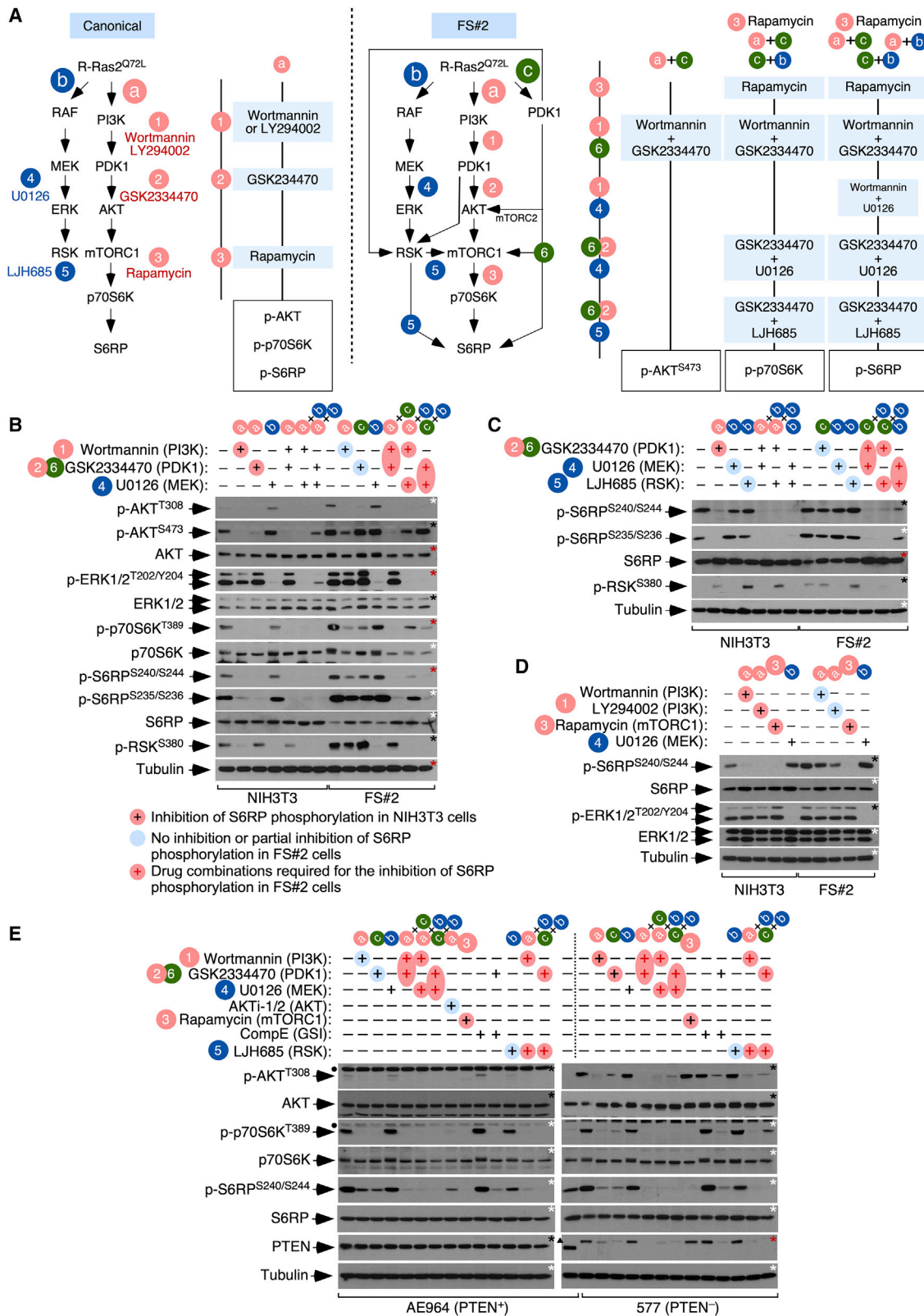
AF820, AF707, AF821, and AF738 cells), indicating that regulation of this kinase follows the canonical PI3Kα-PDK1-AKT pathway in these cells (Figure S6B, right panel). However, phosphorylation of S6RP can only be eliminated in those cells using mTORC1 inhibitors or combinations of PI3K+PDK1 (inputs from the a and c pathways, Figure S6B), PI3K+MEK (inputs from the a and b pathways, Figure S6B), PI3K+RSK (inputs from the a and b pathways, Figure S6B), PDK1+MEK (inputs from pathways a, b, and c, Figure S6B), or PDK1+RSK inhibitors (inputs from pathways a, b, and c, Figure S6B) (Figures 6E and S6A). These results indicate that optimal S6RP phosphorylation needs inputs from the mTORC1, MEK-RSK, and PDK1 pathways (Figure S6B, right panel). We could only find a minor elevation of p-AKT when these cells are incubated with a Notch1 inhibitor (Figures 6E and S6A), suggesting that the synergism observed between R-Ras2^{Q72L} and ICN1 in T leukemogenesis is established at more downstream layers. PTEN$^-$ T-ALL cells exhibit a rather canonical mechanism for phosphorylation of p70S6K and S6RP (see Figure 6E, right panel, for 577 T-ALL cells; see Figure S6C for combined results obtained with 577 and 579 T-ALL cells). These data indicate that R-Ras2^{Q72L} promotes extensive, tumor-cell-specific rewiring of pathways that contribute to stimulation of the mTORC1 pathway (Figures 6A and S6B).

DISCUSSION

In this work, we demonstrated that the long-tail Q72L hotspot mutation of *RRAS2* behaves as a *bona fide* oncogenic driver. Based on these data, our prediction is that this hotspot mutation and other oncogenic *RRAS2* alleles will be identified in a larger number of human tumors when the cancer sequencing projects reach saturation levels for all cancer types. These data also suggest that individuals with *RRAS2* mutant-positive Noonan syndrome will be likely prone to tumor development as they age.

Despite its close structural and signaling similarity with classical Ras proteins, our study has revealed interesting functional differences among those GTPases. Thus, the spectrum of tumors found in iCre-*Rras2*^{Q72L} and oncogenic

Ras mouse models is quite different. For example, tamoxifen-induced iCre-*Rras2*^{Q72L} and *Kras*$^{G12V/+}$ mice only have in common the development of pre-neoplastic (K-Ras$^{G12V/+}$) and fully neoplastic (*Rras2*$^{Q72L/Q72L}$ and *Rras2*$^{Q72L/+}$ mice) lesions in the Harderian glands (Guerra et al., 2003). Oncogenic K-Ras mutants can also promote sarcomas, papillomas, and/or T cell lymphomas like those found in iCre-*Rras2*^{Q72L} mice, but only when expressed from the germline and in a mouse-model-dependent manner (Guerra et al., 2003; Johnson et al., 2001). Conversely, somatic expression of R-Ras2^{Q72L} does not cause the pathologies typically found at high penetrance in Ras subfamily mouse models (Guerra et al., 2003; Hernandez-Porras et al., 2014; Johnson et al., 2001; Karreth and Tuveson, 2009; Schuhmacher et al., 2008). It is unlikely that this different spectrum of tumors is due to differential tissue-specific expression patterns, given that R-Ras2 is widely expressed in mouse tissues (Chan et al., 1994; Larive et al., 2012).

Our study has identified three subclasses of R-Ras2^{Q72L}-driven tumors according to their vulnerability to PI3K and mTORC1 inhibitors. One subclass, which is exclusively composed of ovarian cystadenomas, is heavily dependent on PI3K and mTORC1 activity. This vulnerability probably reflects the implication of R-Ras2^{Q72L} in stimulation of the canonical PI3Kα-AKT-mTORC1 axis in these tumors. Another subclass is composed of tumors whose growth is PI3K and mTORC1 independent. The reason for the therapeutic resistance exhibited by these tumors is unknown. Possible causes include the implication of multiple pathways in the fitness of those tumors, activation of signaling-compensatory mechanisms, or involvement of still unknown effectors. Finally, a third subclass includes highly penetrant pathologies found in iCre-*Rras2*^{Q72L} mice that are exclusively mTORC1 dependent. This suggests that mTORC1 must be activated independent of the PI3K-AKT axis in those tumors. Agreeing with this hypothesis, our studies have revealed that cancer cells from this therapeutic subclass undergo extensive rewiring of the pathways that regulate the signaling output from the mTORC1-S6RP axis (Figures 6A and S6B, right panels). A key nucleator of this process is

Figure 6. R-Ras2^{Q72L} promotes cell-type-specific rewiring of the mTORC1 pathway
(A) Left: schematic of stimulation of the indicated downstream pathways in NIH 3T3 cells. Inhibitors of signaling elements of the PI3K-mTORC1 (a, red color) and ERK (b, blue color) pathways are also shown. The inhibitors required for elimination of phosphorylation of the indicated proteins in these cells are shown on the right side of this panel. Right: schematic of the regulation of the foregoing pathways in FS#2 cells according to results obtained in this work. The alternative PDK1-dependent pathway in these cells (c, green color) and its crosstalk with other routes are indicated. The combinations of inhibitors required for blocking phosphorylation of the indicated proteins is shown on the right side of this panel.
(B–D) Phosphorylation and expression levels of the indicated proteins (left) in NIH 3T3 and FS#2 cells subjected to the indicated experimental conditions (top). As a reference, we indicate the combinations of drugs that must be used to effectively eliminate phosphorylation of S6RP in the two cell types following the codes for pathways (top) and inhibitors (left) described in (A). In addition, we use red circles to indicate the inhibitor (+) or combination of inhibitors (red + sign) needed to effectively inhibit S6RP phosphorylation in NIH 3T3 and FS#2 cells, respectively.
(A–D) The concentrations used in these experiments were as follows: W (A and D, 200 nM), LY294002 (D, 10 μM), GSK2334470 (B and C, 1 μM), R (D, 10 nM), U0126 (B–D, 20 μM), and LJH685 (C, 10 μM). Quantification of these experiments is shown in Figure S5.
(E) Phosphorylation and expression levels of the indicated proteins (left) in the T-ALL cell lines AE964 (PTEN$^-$) and 577 (PTEN$^+$) subjected to the experimental conditions shown at the top. As a reference, we indicate the combinations of drugs that must be used to effectively eliminate phosphorylation of S6RP in the two cell types following the codes for pathways (top) and inhibitors (left) described in Figure S6B. In addition, we use red circles to indicate the inhibitor (+) or combination of inhibitors (red + sign) that are needed to effectively inhibit S6RP phosphorylation in these cells. The concentration for the inhibitors used in these experiments are those indicated in (B)–(D). We also used, in this case, CompE (100 nM) and AKTi-1/2 (5 μM). Quantification of these experiments is shown in Figure S6. Black dots and triangles on the left side of panels indicate nonspecific bands and a remaining signal from the previous immunoblot with antibodies to p-AKT^{S473}, respectively.
See also Figures S5 and S6.

generation of a PI3Kα-independent pool of PDK1 that, depending on the cancer cell type involved, impinges on activation of mTORC1 (FS) and/or S6RP (FS and T-ALL) (Figures 6A and S6B, right panel, pathway c). Our results also indicate that this signaling rewiring is cancer cell type specific. FS cells show the widest remodeling, leading to orthogonal signaling inputs of PI3K, PDK1, and RSK on the mTORC1 pathway (Figure 6A, right panel). This multibranched signaling network has some points of overlap with the recently described PDK1-dependent mechanism that operates in cancer cells resistant to PI3Kα inhibitors (Castel et al., 2016). However, unlike this latter mechanism, R-Ras2^{Q72L}-transformed fibroblasts retain an active PI3Kα-AKT axis and coopt the additional RSK1 signaling branch to regulate mTORC1 output (Figure 6A, right panel). R-Ras2^{Q72L}-transformed T-ALL cells exhibit more limited rewiring because they maintain the canonical PI3Kα-mTORC1-p70S6K lineal pathway intact (although at very low levels of basal activity). However, they retain the inputs from the PI3Kα-independent pool of PDK1 to promote optimal levels of S6RP phosphorylation (Figure S6B, right panel). This small-scale signaling rewiring bears resemblance to the pathway used by *PIK3CA* mutant cancer cells to bypass the negative feedback mechanisms that reduce the signaling output from AKT (Vasudevan et al., 2009). An important inference from the present study is that use of mTORC1 inhibitors or combination therapies that shut off the convergent signals that impinge orthogonally on mTORC1 signaling will likely be the most effective treatments for individuals with cancer and Noonan syndrome bearing oncogenic *RRAS2* mutations (Figures 6A and S6B, left panels).

RalGDS has been linked previously to a large number of RAS-related processes, including cell transformation (for a review, see Ferro and Trabalzini, 2010). In contrast, our study indicates that all R-Ras2^{Q72L}-driven tumors are RalGDS independent. In fact, we unexpectedly found that this Ral guanosine nucleotide exchange factor might have tumor suppressor-like functions during R-Ras2^{Q72L}-mediated transformation of mesenchymal cells. It would be important to verify whether the data obtained here can be reproduced in specific Ras oncogene-driven tumors, such as, for example, FS. It also remains to be investigated whether loss of RalGDS could have an effect on the growth of R-Ras2^{Q72L}-driven tumors when combined with inhibition of other R-Ras2 downstream pathways.

Beyond the limited number of tumors bearing oncogenic *RRAS2* mutations, it is possible that the WT version of R-RAS2 could play more general roles in human tumors because of gene amplification, upregulated expression, enhanced activity, or presence of mutations in upstream and negative regulatory elements in cancer cells. Genetic evidence in favor of the importance of endogenous R-Ras2^{WT} in *Her2*-driven mammary tumorigenesis (Larive et al., 2014), B cell chronic lymphocytic leukemia (Hortal et al., 2022), and Notch1-driven leukemogenesis (this work) is already available for mice. Future studies are needed to better understand the effect of the WT and oncogenic versions of this GTPase in human tumors. The iCre-*Rras2*^{Q72L} mouse strain reported here will also be an ideal tool to preclinically test therapies for individuals with *RRAS2* mutant-positive Noonan syndrome.

Limitations of the study

This work demonstrates that the Q72L mutation of R-RAS2 found in human tumors likely acts as a potent oncogenic driver. However, these data were generated using genetically manipulated mice, and, therefore, we cannot exclude the possibility that the tumorigenic activity of R-RAS2^{Q72L} could be different in human tissue. Likewise, the R-Ras2^{Q72L}-regulated signaling pathways reported here could be further rewired in that setting because of the more complex mutational makeup typically found in human tumors. Other interesting issues that remain to be explored include (1) the genetic lesions and tissue microenvironmental factors that can cooperate with R-Ras2^{Q72L} in cell transformation, (2) the reason underlying the different tumor spectra induced by R-RAS2 and classic RAS oncoproteins, (3) the Achilles' heel (and signaling basis) of R-Ras2^{Q72L}-driven tumors that are PI3K, MEK, and RalGDS independent, (4) the reason for the low frequency of *RRAS2* oncogenic mutations in individuals with cancer and Noonan syndrome.

STAR★METHODS

Detailed methods are provided in the online version of this paper and include the following:

- KEY RESOURCES TABLE
- RESOURCE AVAILABILITY
  - Lead contact
  - Materials availability
  - Data and code availability
- EXPERIMENTAL MODEL AND SUBJECT DETAILS
  - Mouse models
  - Primary tumor cells
  - Primary cells
  - Cell lines
  - Microbe strains
- METHODS DETAILS
  - Histological analyses
  - Immunohistochemistry
  - Flow cytometry determinations
  - Production of viral particles
  - Determination of mRNA abundance
  - Generation of antibodies to R-RAS2
  - Western blotting
  - Cell proliferation assays
  - CRISPR–Cas9-mediated gene knockouts
  - shRNA mediated *Rras2* transcript knockdown
  - Gene expression profiling
  - Bioinformatics of microarray data
- IMMUNOFLUORESCENCE ASSAYS
- QUANTITATION AND STATISTICS
  - Quantitation of phosphorylation levels in immunoblot analyses
  - Quantitation of morphological parameters of fibrosarcoma cells
  - Statistics

SUPPLEMENTAL INFORMATION

Supplemental information can be found online at https://doi.org/10.1016/j.celrep.2022.110522.

AUTHOR CONTRIBUTIONS

I.F.-P. participated in all experimental work, analyzed data, and contributed to artwork design. L.C. carried out work related to the fibrosarcoma cells. J.R.-V. collaborated in bone marrow transplantation experiments. L.F.L.-M. and R.C. carried out *in silico* analyses. B.N. and M.D. helped with the generation of gene-edited cells. A.A., C.G.-M., and M.S.-M. carried out animal work, pathological determinations, and tissue-specific adeno-Cre injections, respectively. C.L.O., A.H., and B.A. generated and characterized the phenotype of Lck-Cre-*Rras2*^Q72L/Q72L mice. D.C. and M.G. collaborated in characterization of T-ALL populations. X.R.B. conceived the work, analyzed data, wrote the manuscript, and carried out the final editing of figures.

DECLARATION OF INTERESTS

The authors declare no competing interests.

INCLUSION AND DIVERSITY

We worked to ensure sex balance in the selection of non-human subjects. One or more of the authors of this paper self-identifies as a member of the LGBTQ+ community. While citing references scientifically relevant for this work, we also actively worked to promote gender balance in our reference list.

REFERENCES

Bailey, M.H., Tokheim, C., Porta-Pardo, E., Sengupta, S., Bertrand, D., Weerasinghe, A., Colaprico, A., Wendl, M.C., Kim, J., Reardon, B., et al. (2018). Comprehensive characterization of cancer driver genes and mutations. Cell *174*, 1034–1035. https://doi.org/10.1016/j.cell.2018.07.034.

Buhrman, G., Holzapfel, G., Fetics, S., and Mattos, C. (2010). Allosteric modulation of Ras positions Q61 for a direct role in catalysis. Proc. Natl. Acad. Sci. U S A *107*, 4931–4936. https://doi.org/10.1073/pnas.0912226107.

Bustelo, X.R., Crespo, P., Fernandez-Pisonero, I., and Rodriguez-Fdez, S. (2018). RAS GTPase-dependent pathways in developmental diseases: old guys, new lads, and current challenges. Curr. Opin. Cell Biol. *55*, 42–51. https://doi.org/10.1016/j.ceb.2018.06.007.

Calvo, F., and Crespo, P. (2009). Structural and spatial determinants regulating TC21 activation by RasGRF family nucleotide exchange factors. Mol. Biol. Cell *20*, 4289–4302. https://doi.org/10.1091/mbc.E09-03-0212.

Capri, Y., Flex, E., Krumbach, O.H.F., Carpentieri, G., Cecchetti, S., Lißewski, C., Rezaei Adariani, S., Schanze, D., Brinkmann, J., Piard, J., et al. (2019). Activating mutations of RRAS2 are a rare cause of noonan syndrome. Am. J. Hum. Genet. *104*, 1223–1232. https://doi.org/10.1016/j.ajhg.2019.04.013.

Castel, P., Ellis, H., Bago, R., Toska, E., Razavi, P., Carmona, F.J., Kannan, S., Verma, C.S., Dickler, M., Chandarlapaty, S., et al. (2016). PDK1-SGK1 signaling sustains AKT-independent mTORC1 activation and confers resistance to PI3Kα inhibition. Cancer Cell *30*, 229–242. https://doi.org/10.1016/j.ccell.2016.06.004.

Castro-Giner, F., Ratcliffe, P., and Tomlinson, I. (2015). The mini-driver model of polygenic cancer evolution. Nat. Rev. Cancer *15*, 680–685. https://doi.org/10.1038/nrc3999.

Chan, A.M., Miki, T., Meyers, K.A., and Aaronson, S.A. (1994). A human oncogene of the RAS superfamily unmasked by expression cDNA cloning. Proc. Natl. Acad. Sci. U S A *91*, 7558–7562.

Chang, M.T., Asthana, S., Gao, S.P., Lee, B.H., Chapman, J.S., Kandoth, C., Gao, J., Socci, N.D., Solit, D.B., Olshen, A.B., et al. (2016). Identifying recurrent mutations in cancer reveals widespread lineage diversity and mutational specificity. Nat. Biotechnol. *34*, 155–163. https://doi.org/10.1038/nbt.3391.

Cox, A.D., Brtva, T.R., Lowe, D.G., and Der, C.J. (1994). R-Ras induces malignant, but not morphologic, transformation of NIH3T3 cells. Oncogene *9*, 3281–3288.

Csibi, A., Lee, G., Yoon, S.O., Tong, H., Ilter, D., Elia, I., Fendt, S.M., Roberts, T.M., and Blenis, J. (2014). The mTORC1/S6K1 pathway regulates glutamine metabolism through the eIF4B-dependent control of c-Myc translation. Curr. Biol. *24*, 2274–2280. https://doi.org/10.1016/j.cub.2014.08.007.

Detwiller, K.Y., Fernando, N.T., Segal, N.H., Ryeom, S.W., D'Amore, P.A., and Yoon, S.S. (2005). Analysis of hypoxia-related gene expression in sarcomas and effect of hypoxia on RNA interference of vascular endothelial cell growth factor A. Cancer Res. *65*, 5881–5889. https://doi.org/10.1158/0008-5472.CAN-04-4078.

Drosten, M., Dhawahir, A., Sum, E.Y., Urosevic, J., Lechuga, C.G., Esteban, L.M., Castellano, E., Guerra, C., Santos, E., and Barbacid, M. (2010). Genetic analysis of Ras signalling pathways in cell proliferation, migration and survival. EMBO J. *29*, 1091–1104. https://doi.org/10.1038/emboj.2010.7.

Ferro, E., and Trabalzini, L. (2010). RalGDS family members couple Ras to Ral signalling and that's not all. Cell Signal. *22*, 1804–1810. https://doi.org/10.1016/j.cellsig.2010.05.010.

Garraway, L.A., and Lander, E.S. (2013). Lessons from the cancer genome. Cell *153*, 17–37. https://doi.org/10.1016/j.cell.2013.03.002.

Graham, S.M., Cox, A.D., Drivas, G., Rush, M.G., D'Eustachio, P., and Der, C.J. (1994). Aberrant function of the Ras-related protein TC21/R-Ras2 triggers malignant transformation. Mol. Cell Biol. *14*, 4108–4115.

Graham, S.M., Oldham, S.M., Martin, C.B., Drugan, J.K., Zohn, I.E., Campbell, S., and Der, C.J. (1999). TC21 and Ras share indistinguishable transforming and differentiating activities. Oncogene *18*, 2107–2116. https://doi.org/10.1038/sj.onc.1202517.

Guerra, C., Mijimolle, N., Dhawahir, A., Dubus, P., Barradas, M., Serrano, M., Campuzano, V., and Barbacid, M. (2003). Tumor induction by an endogenous K-ras oncogene is highly dependent on cellular context. Cancer Cell *4*, 111–120.

Gutierrez, A., Sanda, T., Grebliunaite, R., Carracedo, A., Salmena, L., Ahn, Y., Dahlberg, S., Neuberg, D., Moreau, L.A., Winter, S.S., et al. (2009). High frequency of PTEN, PI3K, and AKT abnormalities in T-cell acute lymphoblastic leukemia. Blood *114*, 647–650. https://doi.org/10.1182/blood-2009-02-206722.

Hernandez-Porras, I., Fabbiano, S., Schuhmacher, A.J., Aicher, A., Canamero, M., Camara, J.A., Cusso, L., Desco, M., Heeschen, C., Mulero, F., et al. (2014). K-RasV14I recapitulates Noonan syndrome in mice. Proc. Natl. Acad. Sci. U S A 111, 16395–16400. https://doi.org/10.1073/pnas.1418126111.

Hinz, B. (2007). Formation and function of the myofibroblast during tissue repair. J. Invest. Dermatol. 127, 526–537. https://doi.org/10.1038/sj.jid.5700613.

Hortal, A.M., Oeste, C.L., Cifuentes, C., Alcoceba, M., Fernández-Pisonero, I., Clavaín, L., Tercero, R., Mendoza, P., Domínguez, V., García-Flores, M., et al. (2022). Overexpression of wild type RRAS2, without oncogenic mutations, drives chronic lymphocytic leukemia. Mol. Cancer 21, 35. https://doi.org/10.1186/s12943-022-01496-x.

Hu, B., and Phan, S.H. (2013). Myofibroblasts. Curr. Opin. Rheumatol. 25, 71–77. https://doi.org/10.1097/BOR.0b013e32835b1352.

Huang da, W., Sherman, B.T., and Lempicki, R.A. (2009). Bioinformatics enrichment tools: paths toward the comprehensive functional analysis of large gene lists. Nucleic Acids Res. 37, 1–13. https://doi.org/10.1093/nar/gkn923.

Huang-da, W., Sherman, B.T., and Lempicki, R.A. (2009). Systematic and integrative analysis of large gene lists using DAVID bioinformatics resources. Nat. Protoc. 4, 44–57.

ICGC/TCGA Pan-Cancer Analysis of Whole Genomes Consortium. (2020). Pan-cancer analysis of whole genomes. Nature 578, 82–93. https://doi.org/10.1038/s41586-020-1969-6.

Johnson, L., Mercer, K., Greenbaum, D., Bronson, R.T., Crowley, D., Tuveson, D.A., and Jacks, T. (2001). Somatic activation of the K-ras oncogene causes early onset lung cancer in mice. Nature 410, 1111–1116. https://doi.org/10.1038/35074129.

Karreth, F.A., and Tuveson, D.A. (2009). Modelling oncogenic Ras/Raf signalling in the mouse. Curr. Opin. Genet. Dev. 19, 4–11. https://doi.org/10.1016/j.gde.2008.12.006.

Larive, R.M., Abad, A., Cardaba, C.M., Hernandez, T., Canamero, M., de Alava, E., Santos, E., Alarcon, B., and Bustelo, X.R. (2012). The Ras-like protein R-Ras2/TC21 is important for proper mammary gland development. Mol. Biol. Cell 23, 2373–2387. https://doi.org/10.1091/mbc.E12-01-0060.

Larive, R.M., Moriggi, G., Menacho-Marquez, M., Canamero, M., de Alava, E., Alarcon, B., Dosil, M., and Bustelo, X.R. (2014). Contribution of the R-Ras2 GTP-binding protein to primary breast tumorigenesis and late-stage metastatic disease. Nat. Commun. 5, 3881. https://doi.org/10.1038/ncomms4881.

Larsen, L.J., and Møller, L.B. (2020). Crosstalk of Hedgehog and mTORC1 pathways. Cells 9, 2316. https://doi.org/10.3390/cells9102316.

Lawrence, M.S., Stojanov, P., Mermel, C.H., Robinson, J.T., Garraway, L.A., Golub, T.R., Meyerson, M., Gabriel, S.B., Lander, E.S., and Getz, G. (2014). Discovery and saturation analysis of cancer genes across 21 tumour types. Nature 505, 495–501. https://doi.org/10.1038/nature12912.

Li, X., Gounari, F., Protopopov, A., Khazaie, K., and von Boehmer, H. (2008). Oncogenesis of T-ALL and nonmalignant consequences of overexpressing intracellular NOTCH1. J. Exp. Med. 205, 2851–2861. https://doi.org/10.1084/jem.20081561.

López-Barahona, M., Bustelo, X.R., and Barbacid, M. (1996). The TC21 oncoprotein interacts with the Ral guanosine nucleotide dissociation factor. Oncogene 12, 463–470.

Martinez-Martin, N., Fernandez-Arenas, E., Cemerski, S., Delgado, P., Turner, M., Heuser, J., Irvine, D.J., Huang, B., Bustelo, X.R., Shaw, A., and Alarcon, B. (2011). T cell receptor internalization from the immunological synapse is mediated by TC21 and RhoG GTPase-dependent phagocytosis. Immunity 35, 208–222. https://doi.org/10.1016/j.immuni.2011.06.003.

Mata, D.A., Yang, S.R., Ferguson, D.C., Liu, Y., Sharma, R., Benhamida, J.K., Al-Ahmadie, H.A., Chakravarty, D., Solit, D.B., Tickoo, S.K., et al. (2020). RAS/MAPK pathway driver alterations are significantly associated with oncogenic KIT mutations in germ-cell tumors. Urology 144, 111–116. https://doi.org/10.1016/j.urology.2020.07.027.

Michaloglou, C., Crafter, C., Siersbaek, R., Delpuech, O., Curwen, J.O., Carnevalli, L.S., Staniszewska, A.D., Polanska, U.M., Cheraghchi-Bashi, A.,

Lawson, M., et al. (2018). Combined inhibition of mTOR and CDK4/6 is required for optimal blockade of E2F function and long-term growth inhibition in Estrogen receptor-positive breast cancer. Mol. Cancer Ther. 17, 908–920. https://doi.org/10.1158/1535-7163.MCT-17-0537.

Movilla, N., Crespo, P., and Bustelo, X.R. (1999). Signal transduction elements of TC21, an oncogenic member of the R-Ras subfamily of GTP-binding proteins. Oncogene 18, 5860–5869. https://doi.org/10.1038/sj.onc.1202968.

Niihori, T., Nagai, K., Fujita, A., Ohashi, H., Okamoto, N., Okada, S., Harada, A., Kihara, H., Arbogast, T., Funayama, R., et al. (2019). Germline-activating RRAS2 mutations cause noonan syndrome. Am. J. Hum. Genet. 104, 1233–1240. https://doi.org/10.1016/j.ajhg.2019.04.014.

Ohba, Y., Mochizuki, N., Yamashita, S., Chan, A.M., Schrader, J.W., Hattori, S., Nagashima, K., and Matsuda, M. (2000). Regulatory proteins of R-Ras, TC21/R-Ras2, and M-Ras/R-Ras3. J. Biol. Chem. 275, 20020–20026. https://doi.org/10.1074/jbc.M000981200.

Reich, M., Liefeld, T., Gould, J., Lerner, J., Tamayo, P., and Mesirov, J.P. (2006). GenePattern 2.0. Nat. Genet. 38, 500–501. https://doi.org/10.1038/ng0506-500.

Ritchie, M.E., Phipson, B., Wu, D., Hu, Y., Law, C.W., Shi, W., and Smyth, G.K. (2015). Limma powers differential expression analyses for RNA-sequencing and microarray studies. Nucleic Acids Res. 43, e47. https://doi.org/10.1093/nar/gkv007.

Rosario, M., Paterson, H.F., and Marshall, C.J. (1999). Activation of the Raf/MAP kinase cascade by the Ras-related protein TC21 is required for the TC21-mediated transformation of NIH 3T3 cells. EMBO J. 18, 1270–1279. https://doi.org/10.1093/emboj/18.5.1270.

Rosario, M., Paterson, H.F., and Marshall, C.J. (2001). Activation of the Ral and phosphatidylinositol 3' kinase signaling pathways by the ras-related protein TC21. Mol. Cell Biol. 21, 3750–3762. https://doi.org/10.1128/MCB.21.11.3750-3762.2001.

Rouillard, A.D., Gundersen, G.W., Fernandez, N.F., Wang, Z., Monteiro, C.D., McDermott, M.G., and Ma'ayan, A. (2016). The harmonizome: a collection of processed datasets gathered to serve and mine knowledge about genes and proteins. Database (Oxford) 2016, baw100. https://doi.org/10.1093/database/baw100.

Roy, E., Togbe, D., Holdorf, A., Trubetskoy, D., Nabti, S., Küblbeck, G., Schmitt, S., Kopp-Schneider, A., Leithäuser, F., Möller, P., et al. (2010). Fine tuning of the threshold of T cell selection by the Nck adapters. J. Immunol. 185, 7518–7526. https://doi.org/10.4049/jimmunol.1000008.

Scheidig, A.J., Burmester, C., and Goody, R.S. (1999). The pre-hydrolysis state of p21(ras) in complex with GTP: new insights into the role of water molecules in the GTP hydrolysis reaction of ras-like proteins. Structure 7, 1311–1324. https://doi.org/10.1016/s0969-2126(00)80021-0.

Scholl, C., and Fröhling, S. (2019). Exploiting rare driver mutations for precision cancer medicine. Curr. Opin. Genet. Dev. 54, 1–6. https://doi.org/10.1016/j.gde.2019.02.004.

Schuhmacher, A.J., Guerra, C., Sauzeau, V., Canamero, M., Bustelo, X.R., and Barbacid, M. (2008). A mouse model for Costello syndrome reveals an Ang II-mediated hypertensive condition. J. Clin. Invest. 118, 2169–2179. https://doi.org/10.1172/JCI34385.

Schulte, S.L., Waha, A., Steiger, B., Denkhaus, D., Dörner, E., Calaminus, G., Leuschner, I., and Pietsch, T. (2016). CNS germinomas are characterized by global demethylation, chromosomal instability and mutational activation of the Kit-, Ras/Raf/Erk- and Akt-pathways. Oncotarget 7, 55026–55042. https://doi.org/10.18632/oncotarget.10392.

Silva, A., Yunes, J.A., Cardoso, B.A., Martins, L.R., Jotta, P.Y., Abecasis, M., Nowill, A.E., Leslie, N.R., Cardoso, A.A., and Barata, J.T. (2008). PTEN post-translational inactivation and hyperactivation of the PI3K/Akt pathway sustain primary T cell leukemia viability. J. Clin. Invest. 118, 3762–3774. https://doi.org/10.1172/JCI34616.

Simanshu, D.K., Nissley, D.V., and McCormick, F. (2017). RAS proteins and their regulators in human disease. Cell 170, 17–33. https://doi.org/10.1016/j.cell.2017.06.009.

Su, S., Law, C.W., Ah-Cann, C., Asselin-Labat, M.L., Blewitt, M.E., and Ritchie, M.E. (2017). Glimma: interactive graphics for gene expression analysis. Bioinformatics 33, 2050–2052. https://doi.org/10.1093/bioinformatics/btx094.

Subramanian, A., Tamayo, P., Mootha, V.K., Mukherjee, S., Ebert, B.L., Gillette, M.A., Paulovich, A., Pomeroy, S.L., Golub, T.R., Lander, E.S., and Mesirov, J.P. (2005). Gene set enrichment analysis: a knowledge-based approach for interpreting genome-wide expression profiles. Proc. Natl. Acad. Sci. U S A. 102, 15545–15550. https://doi.org/10.1073/pnas.0506580102.

Tomasek, J.J., Gabbiani, G., Hinz, B., Chaponnier, C., and Brown, R.A. (2002). Myofibroblasts and mechano-regulation of connective tissue remodelling. Nat. Rev. Mol. Cell Biol. 3, 349–363. https://doi.org/10.1038/nrm809.

Van Vlierberghe, P., and Ferrando, A. (2012). The molecular basis of T cell acute lymphoblastic leukemia. J. Clin. Invest. 122, 3398–3406. https://doi.org/10.1172/JCI61269.

Vasudevan, K.M., Barbie, D.A., Davies, M.A., Rabinovsky, R., McNear, C.J., Kim, J.J., Hennessy, B.T., Tseng, H., Pochanard, P., Kim, S.Y., et al. (2009). AKT-independent signaling downstream of oncogenic PIK3CA mutations in human cancer. Cancer Cell 16, 21–32. https://doi.org/10.1016/j.ccr.2009.04.012.

Winbanks, C.E., Grimwood, L., Gasser, A., Darby, I.A., Hewitson, T.D., and Becker, G.J. (2007). Role of the phosphatidylinositol 3-kinase and mTOR pathways in the regulation of renal fibroblast function and differentiation. Int. J. Biochem. Cell Biol. 39, 206–219. https://doi.org/10.1016/j.biocel.2006.08.004.

Wu, C.C., Hou, S., Orr, B.A., Kuo, B.R., Youn, Y.H., Ong, T., Roth, F., Eberhart, C.G., Robinson, G.W., Solecki, D.J., et al. (2017). mTORC1-Mediated inhibition of 4EBP1 is essential for Hedgehog signaling-driven translation and medulloblastoma. Dev. Cell 43, 673–688.e5. https://doi.org/10.1016/j.devcel.2017.10.011.

Yuan, T.L., Amzallag, A., Bagni, R., Yi, M., Afghani, S., Burgan, W., Fer, N., Strathern, L.A., Powell, K., Smith, B., et al. (2018). Differential effector engagement by oncogenic KRAS. Cell Rep. 22, 1889–1902. https://doi.org/10.1016/j.celrep.2018.01.051.

Zhang, X., Spiegelman, N.A., Nelson, O.D., Jing, H., and Lin, H. (2017). SIRT6 regulates Ras-related protein R-Ras2 by lysine defatty-acylation. Elife 6, e25158. https://doi.org/10.7554/eLife.25158.

STAR★METHODS

KEY RESOURCES TABLE

REAGENT or RESOURCE	SOURCE	IDENTIFIER
Antibodies		
Anti-R-Ras2 rabbit antibody (C-terminus)	Customer-made at Invitrogen services	Ref#1234
Anti-α-tubulin mouse antibody, Clone DM1A	Calbiochem	Cat# CP06 RRID:AB_2617116
Anti-phospho-p44/42 MAPK (Erk1/2) (Thr202/Tyr204) rabbit antibody	Cell Signaling Technology	Cat# 4370 RRID:AB_2315112
Anti-p44/42 MAPK (Erk1/2) antibody	Cell Signaling Technology	Cat# 9102 RRID:AB_330744
Anti-Phospho-AKT (Thr308) (244F9) rabbit antibody	Cell Signaling Technology	Cat# 4056 RRID:AB_331163
Anti-Phospho-AKT (Ser473) (587F11) mouse antibody	Cell Signaling Technology	Cat# 4051 RRID:AB_331158
Anti-total AKT (40D4) mouse antibody	Cell Signaling Technology	Cat# 2920 RRID:AB_1147620
Anti-PTEN rabbit antibody, Biotin conjugated, Clone 138G6	Cell Signaling Technology	Cat# 9583 RRID:AB_2174346
Anti-phospho-p70 S6 kinase (Thr389) antibody	Cell Signaling Technology	Cat# 9205 RRID:AB_330944
Anti-phospho-p70 S6 kinase (Thr421/Ser424) antibody	Cell Signaling Technology	Cat# 9204 RRID: AB_2265913
Anti-phospho S6 ribosomal protein (Ser240/Ser244) antibody	Cell Signaling Technology	Cat# 2215 RRID:AB_331682
Anti-phospho S6 ribosomal protein (Ser235/Ser236) antibody	Santa Cruz Biotechnology	Cat# sc-293144 RRID:AB_2895113
Anti-p70 S6 kinase antibody, Clone C-18	Santa Cruz Biotechnology	Cat# sc-230 RRID:AB_632156
Anti-phospho-RSK (Ser380) antibody	Santa Cruz Biotechnology	Cat# sc-377526
Anti-rabbit anti-RPS6 antibody, affinity purified	Bethyl laboratories	Bethyl Cat# A300-557A, RRID:AB_477988
Rat anti-mouse CD4 antibody, APC-H7 conjugated, Clone GK1.5	BD Biosciences	Cat# 560181; RRID: AB_1645235
Rat anti-Mouse CD8a, FITC conjugated, Clone 53-6.7	BD Biosciences	Cat# 553031; RRID:AB_394569
Pacific Blue™ rat anti-mouse CD8a, Clone 53 6.7	BD Biosciences	Cat# 558106; RRID:AB_397029
PE rat anti-mouse CD8a, Clone 53-6.7	BD Biosciences	Cat# 553032 RRID:AB_2034011
APC rat anti-mouse CD25, Clone 3C7	BD Biosciences	Cat# 558643 RRID:AB_1645222
PE-Cy™7 rat anti-mouse CD25, Clone PC61	BD Biosciences	Cat# 552880 RRID: AB_394509
APC rat anti-mouse CD24 monoclonal antibody, Clone M1/69	eBioscience	Cat# 17-0242-82 RRID: AB_10870773
PerCP-Cy5.5-labeled antibody to CD44	BD Biosciences	Cat# 560570 RRID: AB_1727486
PerCP-Cyanine5.5 anti-mouse CD45R (B220) monoclonal antibody, Clone RA3-6B2	eBioscience	Cat# 45-0452-82 RRID:AB_1107006
PE anti-mouse TCRβ monoclonal antibody, Clone H57-597	eBioscience	Cat# 12-5961-82 RRID:AB_466066
PE-labeled antibody to phospho-AKT (pS473)	BD Biosciences	Cat# 560378 RRID:AB_1645328
PE anti-mouse Notch1 monoclonal antibody, Clone mN1A	eBioscience	Cat# 552768 RRID:AB_394454
Anti-cleaved Notch1 (Val1744) (D3B8) antibody	Cell Signaling Technology	Cat# 4147 RRID:AB_2153348
Anti-α-smooth muscle actin	Sigma-Aldrich	Cat# A2547 RRID: AB_476701
Goat anti-mouse IgG (H+L) highly cross-adsorbed secondary antibody, Alexa Fluor 594 conjugated	Thermo Fisher Scientific	Cat# A-11032 RRID:AB_2534091

(Continued on next page)

Continued

REAGENT or RESOURCE	SOURCE	IDENTIFIER
Rhodamine conjugated phalloidin antibody	Thermo Fisher Scientific	Cat# R415 RRID:AB_2572408
Goat anti-rabbit IgG (H+L) cross-adsorbed secondary antibody, Alexa Fluor 488 conjugated	Invitrogen	Cat# A-32723 RRID: AB_2633275
Chicken anti-mouse IgG (H+L) highly cross-adsorbed secondary antibody, Alexa Fluor Plus 647 conjugated	Invitrogen	Cat# A-21443 RRID:AB_2535861
Anti-vimentin antibody	Cell Marque	Cat# 347R-15, RRID:AB_2335639
Anti-rat anti-CD117 monoclonal antibody, allophycocyanin conjugated, Clone 2B8	BD Biosciences	Cat# 553356; RRID:AB_398536
Bacterial and virus strains		
DH5α competent *E. coli* cells	Homemade	N/A
Chemicals, peptides, and recombinant proteins		
TripLE™ Express	GIBCO	Cat# 12604013
MTT Formazan	Sigma-Aldrich	Cat# M2128-5G
Isoflurane (Vetflurane)	Virbac	Cat# 575837-4
Fast green FCF	Sigma-Aldrich	Cat# F7258
Buprex (Buprenorphin)	Reckitt Benckiser	Cat# 679588
Tamoxifen	Sigma-Aldrich	Cat# T5648
BD Cytofix/Cytoperm™	BD Biosciences	Cat# 554714; RRID:AB_286900
NZYol	NZYtech	Cat# MB18501
ETP-46321	Dr. Joaquin Pastor Lab	N/A
ETP-992	Dr. Joaquin Pastor Lab	N/A
Rapamycin (Sirolimus)	Selleckchem	Cat# S1039
PD0325901	Selleckchem	Cat# S1036
PEG300	Sigma-Aldrich	Cat# 202371
N-methyl-pyrrolidone	Sigma-Aldrich	Cat# 443778
Hydroxypropyl methylcellulose	Sigma-Aldrich	Cat# 09963
Tween 80	Sigma-Aldrich	Cat# P8074
Dynabeads™ biotin binder	Invitrogen	Cat# 11047
RetroNectin	Takara	Cat# T100A
Murine SCF	Peprotech	Cat# 500-P71
hrFlt3	Peprotech	Cat# 300-19
hrTPO	Peprotech	Cat# AF-300-18
hrIL-6	Peprotech	Cat# 200-06
Polybrene	Sigma-Aldrich	Cat# H9268
Matrigel matrix	BD Biosciences	Cat# 354234
Puromycin	Sigma-Aldrich	Cat# P8833
N-methyl-pyrrolidone	Sigma-Aldrich	Cat# 443778
Compound E (γ-secretase inhibitor)	Alexis Biochemicals	Cat# ALX-270-415
PDGF-BB	Peprotech	Cat# 315-18
Wortmannin	Selleckchem	Cat# S2758
GSK2334470	Selleckchem	Cat# S7087
U0126	Selleckchem	Cat# S1102
Rapamycin	Selleckchem	Cat# S1039
Fibronectin	Roche	Cat# 10838039001
LJH685	Selleckchem	Cat# S7870
LY294002	Selleckchem	Cat# S1105
AKTi-1/2	Selleckchem	Cat# S7776

(Continued on next page)

Continued

REAGENT or RESOURCE	SOURCE	IDENTIFIER
Critical commercial assays		
RNAeasy Mini Kit	Qiagen	Cat# 74104
Lipofectamine 2000	ThermoFisher Scientific	Cat# 11668019
Purelink™ Genomic DNA Mini kit	Invitrogen	Cat# K182002
JetPEI transfection reagent	Polyplus	Cat# 101-10N
Bradford reagent	Bio-rad	Cat# 5000006
ECL Pierce	Thermo	Cat# 32106
Power SYBR Green RNA-to-CT 1-Step Kit	Applied Biosystems	Cat# 4389986
Anti-mouse lineage cell detection cocktail antibody, Biotin conjugated	Miltenyi Biotec	Cat# 130-092-613 RRID:AB_1103214
Deposited data		
Microarray data	This study	GEO: GSE179409
Microarray data	Detwiller et al., 2005	GEO: GSE2719
Harmonizome database	Rouillard et al., 2016	https://maayanlab.cloud/Harmonizome/
Molecular signatures database (MSigDB v7.2)	Broad Institute	https://software.broadinstitute.org/cancer/software/gsea/wiki/index.php/MSigDB_v7.2_Release_Notes
Experimental models: Cell lines		
Mouse: OP9-DL1 (sex unknown)	Dr. M.L. Toribio's lab	N/A
Mouse: fibrosarcoma cell lines (e.g., FS#2; female)	This study	N/A
Mouse: T-ALL cell clones (9 male, 3 female)	This study	N/A
Human: HEK293 (female)	ATCC	Cat# CRL-1573 RRID:CVCL_0045
Mouse: NIH3T3 (male)	ATCC	Cat# CRL-1658 RRID:CVCL_0594
Mouse embryonic fibroblasts (primary, mixed sex)	This study	N/A
Experimental models: Organisms/strains		
Mouse: iCre-*Rras2*^{Q72L} (C57BL/6)	This study	N/A
Mouse: iCre-*Rras2*^{Q72L};*Ralgds*$^{-/-}$ (C57BL/6)	This study	N/A
Mouse: Lck-Cre-*Rras2*^{Q72L} (C57BL/6J)	This study	N/A
Mouse: *Rras2*$^{-/-}$ (C57BL/6J)	Larive et al., 2012	N/A
Oligonucleotides		
See Table S2		N/A
Recombinant DNA		
pSpCas9(BB)-2A-GFP	Addgene	Cat# 48138
pICN1-GFP	Dr. M.L. Toribio's lab	N/A
pX330-U6-Chimeric_BB-CBh-hSpCas9	Addgene	Cat# 42230
mTC21 sgRNA1 (pMFP23)	This study	N/A
mTC21 sgRNA2 (pMFP24)	This study	N/A
pBlueScript II SK ii (+)	Addgene	Cat# 212205
pBlueScript II SK ii (+) + EGFP (pJG1)	This study	N/A
pJG1 + mTC21 homol left/right (pMFP29)	This study	N/A
pEGFP-N3	Addgene	Cat# 6080-1
pMFP29 + polyA (pMFP34)	This study	N/A
pTR1.5-pLKO-1-puro (scrambled)	Sigma-Aldrich	Cat# SHC001
Rras2-directed shRNA (sh1)	Sigma-Aldrich	Cat# TRCN0000311478
Rras2-directed shRNA (sh2)	Sigma-Aldrich	Cat# TRCN0000077751

(Continued on next page)

REAGENT or RESOURCE	SOURCE	IDENTIFIER
Rras2-directed shRNA (sh3)	Sigma-Aldrich	Cat# TRCN0000077752
Rras2-directed shRNA (sh4)	Sigma-Aldrich	Cat# TRCN0000354089
pEGFP-Rras2 Q72L	This study	N/A
pMD2.G	Addgene	Cat#12259
psPax2	Addgene	Cat#12260
Software and algorithms		
FlowJo (version 8.7.3)	FlowJo, LLC	https://www.flowjo.com/solutions/flowjo
StepOne (version 2.1)	ThermoFisher Scientific	https://www.thermofisher.com/order/catalog/product/4376600
ImageJ (version 1.44p)	NIH Image	https://imagej.nih.gov/ij/
GraphPad Prism (version 6.0)	GraphPad Software Inc	https://www.graphpad.com/scientific-software/prism/
Benchling CRISPR design tool	Benchling	www.benchling.com
R (version 3.6.3)	R Core Team	https://stat.ethz.ch/pipermail/r-announce/2020/000650.html
Python (version 3.8.0)	Python	https://www.python.org/downloads/release/python-390/
RMA	Bioconductor	http://bioconductor.org/packages/release/bioc/html/affy.html
Limma	Ritchie et al., 2015	https://bioconductor.org/packages/release/bioc/html/limma.html
DAVID	Huang da et al., 2009; Huang-da et al., 2009	https://david.ncifcrf.gov
Heatmap3	The Comprehensive R Archive Network	http://CRAN.R-project.org/package=heatmap3
Glimma R	Su et al., 2017	https://bioconductor.org/packages/release/bioc/html/Glimma.html
GSEA	Subramanian et al., 2005	http://software.broadinstitute.org/gsea/index.jsp
ssGSEA	Reich et al., 2006; Subramanian et al., 2005	https://genepattern.broadinstitute.org/gp/pages/login.jsf

RESOURCE AVAILABILITY

Lead contact
Further information and requests for resources and reagents should be directed to and will be fulfilled by the lead contact, Xosé R. Bustelo (xbustelo@usal.es).

Materials availability
All unique reagents generated in this study are available from the lead contact without restriction for academic research use. A materials transfer agreement could be required in the case of potential commercial applications.

Data and code availability
- Microarray data generated in this paper have been deposited in the GEO database and are publicly available as of the date of publication. This study has also used genome-wide expression data reported by other studies. Accession numbers for all those datasets are indicated in the key resources table. A Source Data file (including original Western blot data) is provided as an online resource with this paper. Microscopy data reported in this work will be shared by the lead contact upon request.
- This paper does not report original code.
- Any additional information required to reanalyze the data reported in this paper is available from the lead contact upon request.

EXPERIMENTAL MODEL AND SUBJECT DETAILS

Mouse models

All mouse experiments were performed according to protocols approved by the Bioethics Committee of the University of Salamanca and the animal experimentation authorities of the autonomous government of Castilla y León (Spain).

The iCre-*Rras2*^{Q72L} knock-in mouse strain was generated by GenOway (www.genoway.com) using the vector indicated in Figure S1 following standard homologous recombination techniques in mouse embryonic stem cells. Upon generation of mice from embryonic stem cells, the subsequent steps involved further crosses with transgenic mice to induce the removal of the *Neo*^{R} cassette (using a Flippase-expressing mouse strain) and to generate the tamoxifen-inducible model (using the mice expressing Cre-ER^{T2} under the regulation of the endogenous ubiquitin promoter) (Figure S1A and S1B). Routine genotyping was performed by PCR using primers targeting the upstream sequence to the 5′ *Lox*511 (5′-GCCAAAGAGACATGCAGTGAGAAGAGTACC-3′) and the 3′ *Lox*511/*Lox*P tandem sites (5′-CCACCATGAGTCCAATGATTGCACC-3′). For the genotyping of the knock-in lines, the F$_2$ progeny was screened by PCR amplification using primers specific for the wild-type *Rras2* allele which anneal upstream and downstream of exon 3, respectively (forward primer: 5′-TTTAGAGTTGATTTGGTTCCATCTGCTTGG-3′; reverse primer: 5′-CCATAAAATAG-CAATCTGGACAGAACCTAGCA-3′). Cre recombinase-encoding sequences were also detected by PCR (forward primer: 5′-CCGGTTATTCAACTTGCACC-3′; reverse primer: 5′-CTGCATTACCGGTCGATGCAAC-3′). To generate Lck-Cre-*Rras2*^{Q72L} mice, Lck-Cre-*Nck1*$^{-/-}$*Nck2*$^{flx/flx}$ mice (Roy et al., 2010) were back-crossed with C57BL/6 animals to obtain single Lck-Cre mice. These mice were then crossed with iCre-*Rras2*$^{Q72L/Q72L}$ mice to obtain the final Lck-Cre-*Rras2*^{Q72L} strain. To generate iCre-*Rras2*^{Q72L};*Ralgds*$^{-/-}$ mice, frozen sperm from *Ralgds*$^{-/-}$ mice obtained from Dr. A. McCarthy (Division of Cancer Biology, The Institute of Cancer Research, London, UK) was used to fertilize ovules of iCre-*Rras2*$^{Q72L/Q72L}$ and C57BL/6 mice at the University of Salamanca Animal Facility. The founder mice were subsequently crossed with wild-type C57BL/6 mice to generate the F$_1$ generation bearing the mutant alleles. Further crosses were performed to obtain a fully clean strain in the C37BL/6 genetic background. Genotyping was performed by PCR using a common forward primer for the detection of WT and KO versions of *Ralgds* (5′-GAAGGT-GAGGTGCACAAAGGCC-3′) and a reverse primer for either the WT (5′-CATCTCCAGTGTGGCAAACTTGG-3′) or the KO (5′-GATGA-CAGTCGGAGCCTTATCC-3′) version.

To induce the somatic expression of endogenous R-Ras2^{Q72L}, we injected 100 μL of tamoxifen (10 mg/mL resuspended in 10% ethanol and diluted in 90% sunflower oil; Cat. No. T5648-5G, Sigma-Aldrich) intraperitoneally every 24 h for 5 consecutive days in one-month-old iCre-*Rras2*$^{Q72L/Q72L}$, iCre-*Rras2*$^{Q72L/+}$ or control mice. Mice were then examined weekly until showing obvious physical signs of sickness. Upon euthanasia, the indicated tissues and peripheral blood samples were collected and processed as indicated. For the treatment with inhibitors, we used the following conditions: PD0325901 (Cat. No. S1036, Selleckchem) dissolved in 0.5% hydroxypropyl methylcellulose [Cat. No. 09963, Sigma-Aldrich] and 0.2% Tween-80 [Cat. No. P8074, Sigma-Aldrich]) was administered at 5 mg/Kg (100 μL) five days per week by oral gavage. Rapamycin (Sirolimus, Cat. No. S1039, Selleckchem) dissolved in 5% polyethylene glycol 300 [Cat. No. 202371, Sigma-Aldrich] plus 5% Tween-80 was administered five days per week by intraperitoneal injection using a concentration of 5 mg/Kg (80 μL). ETP-992 and ETP-46321 (provided by J. Pastor, CNIO, Madrid, Spain) dissolved in 10% N-methyl-pyrrolidone [Cat. No. 443778, Sigma-Aldrich] and 90% polyethylene glycol 300 were administered by oral gavage five days per week at concentration of 20 mg/Kg (100 μL) and 50 mg/Kg (100 μL), respectively. All the treatments were administered during the time indicated in the figures.

For the tissue-specific expression of R-Ras2^{Q72L}, adenoviral particles encoding different versions of Cre (Ad5CMVCre-eGFP, Cat. No. VVC-U of Iowa-1174; Ad5CMVCre, Cat. No. VVC-U of Iowa-5) were generated at the University of Iowa Viral Vector Core Facility. For expression in bladder, the organ was accessed via ventral incision and the solution containing the adenoviral particles (2 × 10^8 pfu in 5 μL) delivered using a 30-gauge beveled glass needle under the control of a dissecting microscope. The virus solution contained fast green FCF 0.1% in phosphate-buffered saline solution to follow up proper injection of the viral particles in the tissue wall. Mice were kept under deep anesthesia with isoflurane. For expression in uteri, the uterine horns were ligated with suture at the base to prevent leakage of the viral solution into the vagina. Subsequently, 10 μL of the viral solution (2 × 10^8 pfu) were injected in the uterus as above. At the indicated times, the tissues were harvested, fixed in 10% formalin, paraffin embedded, sectioned. and stained for histological analyses. For expression in the lung epithelium, 50 μL of the adenoviral solution (2.5 × 10^7 pfu/animal resuspended in complete RPMI and precipitated with 10 mM CaCl$_2$ for 20 minutes) was inserted into the nostril of the experimental mice. In this case, mice were anesthetized with a combination of 10 μL/g of Diazepam (5 mg/mL Valium, Roche), 25 μL of atropine (1 mg/mL, Cat No. 436112, Braun), 62.5 μL of ketamine (11.25 g/100 mL Imalgene 1000, Cat No. 571267.3, Merial) and 812.5 μL of physiological serum (Cat. No. 999791.5, ERN). For expression in subcutaneous areas, 10 μL of the viral solution (2 × 10^8 pfu) diluted in 40 μL of phosphate buffered solution was injected in the dermis of a selected area of the back skin. At the indicated times, the tissues were harvested, fixed in 10% formalin, paraffin embedded, sectioned, and stained for histological analyses.

Animals used were of both sexes and ranged in age from 0 to the time of euthanasia indicated in the main text. Experimental groups were assigned randomly.

Primary tumor cells

In the case of leukemic cells (derived both from male and female animals), single cell suspensions were generated by mechanical homogenization of either the thymus or the spleen from tamoxifen-treated iCre-*Rras2*^{Q72L} mice in 3 mL of phosphate-buffered saline

solution supplemented with 2% bovine serum albumin (Cat. No. A4503, Sigma-Aldrich) plus 0.5 mM EDTA (referred to hereafter as cell extraction buffer), washed once by low-speed centrifugation, and subjected to erythrocyte lysis using the ACK buffer (150 mM NH₄Cl, 10 mM KHCO₃ [pH 7.3], 0.1 mM Na₂EDTA). Cells were then cultured with feeder layers of OP9-DL1 cells. For transplantation experiments, 500,000 cells were intravenously injected into recipient WT mice. Fibrosarcoma cell lines were obtained by explanting the tumors collected from female iCre-*Rras2*^{Q72L} mice in DMEM supplemented with 10% fetal bovine serum. When indicated, cells were treated with Compound E (100 nM, Cat. No. ALX-270-415, Enzo), Rapamycin (10 nM), Wortmannin (200 nM, Cat. No. S2758, Selleckchem), U0126 (20 μM), GSK2334470 (1 μM, Cat. No. S7087, Selleckchem), LJH685 (10 μM, Cat. No. S7870, Selleckchem), LY294002 (10 μM, Cat. No. S1105, Selleckchem), AKTi-1/2 (5 μM, Cat. No. S7776, Selleckchem) or vehicle alone (DMSO) and then collected 2 h later. When indicated, fibrosarcoma cells were serum starved for 4 h and then stimulated with PDGF-BB (10 nM, Cat. No. 315-18, Peprotech) for the times indicated in figures.

For the subcutaneous xenograft experiments, exponentially growing fibrosarcoma cells were collected and resuspended in a mixture with phosphate-buffered saline solution and Matrigel (Cat. No. 354234, BD Biosciences) at 1:1 ratio and a concentration of 5 × 10⁶ cells/mL. 100 μL of this cell suspension were then injected subcutaneously into the back of the mice (100 μL). Mice were monitored weekly until showing obvious signs of pain and distress. Upon euthanasia, tissues were collected and fixed for hematoxylin and eosin staining.

Primary cells

Bone marrow cells were freshly collected by flushing the femur and tibia cavities of the hind legs of male mice of the indicated genotypes with cell extraction buffer, washed once by low-speed centrifugation, resuspended in cell extraction buffer, subjected to lysis with ACK buffer, and filtered with a cell strainer (nylon mesh with 40-μm pores, Cat. No. 352340, Falcon) to remove debris. Lin-negative bone marrow cells were then purified by negative selection using the Lineage Cell Detection Cocktail-Biotin kit (Cat. No. 130-092-613, Miltenyi Biotec) followed by depletion with Dynabeads™ Biotin Binder (Cat. No. 11047, Invitrogen) according to the manufacturer's protocol. Subsequently, c-Kit⁺ cells were isolated from the Lin-negative cell suspension by sorting using a FACSAria III flow cytometer. 1 × 10⁶ of purified c-Kit⁺ bone marrow cells were then cultured on RetroNectin (Cat. No. T100A, Takara; 50 μg/mL)-coated plate for 4 h in RPMI-1640 containing 10% fetal bovine serum, glutamine, and a mix of cytokines (50 IU/mL murine SCF [Cat. No. 500-P71, Peprotech], 50 IU/mL hrFlt3 [Cat. No. 300-19, Peprotech], 50 IU/mL hrTPO [Cat. No. AF-300-18, Peprotech] and 25 IU/mL of hrIL-6 [Cat. No. 200-06, Peprotech]). Upon stimulation, the bone marrow precursors were infected with lentiviral particles and pelleted by centrifugation (1,800 xg for 90 min). The transduction efficiency was examined by flow cytometry 24 h after the transduction step. Transduced cells were then used for bone marrow transplantation experiments as indicated below. EGFP⁺ c-Kit⁺ cells were then collected by centrifugation (1,500 xg for 10 min) and resuspended in phosphate-buffered saline solution at a concentration of 1 × 10⁶ cells/mL. 100 μL of the cell resuspension were then introduced by tail vein injection into 6- to 8-week-old irradiated-recipient male WT mice (lethal dose of 10 Gy). Mice were examined weekly after the transplantation step until showing obvious physical signs of sickness or discomfort. Aliquots of peripheral blood (100 μL) were analyzed by flow cytometry to detect changes in immune populations. Upon euthanasia, the indicated tissues and peripheral blood were collected for further analyses.

Cell lines

NIH3T3 (Cat. No. CRL-1658, male) and HEK293T (Cat. No. CRL-1573, female) cells were obtained from the American Type Culture Collection and maintained in DMEM (Dulbecco's Modified Eagle Medium) supplemented with 10% fetal bovine serum plus penicillin (10 μg/mL) and streptomycin (100 μg/mL). Bone marrow stromal cells overexpressing either GFP (OP9-GFP, unknown sex) or the Delta-like 1 protein (OP9-DL1) were provided by Dr. M.L. Toribio (Centro de Biología Molecular Severo Ochoa, CSIC, Madrid, Spain). These cells were grown in MEM (minimal essential media) α medium supplemented with 20% fetal bovine serum plus antibiotics as above. All cell lines were maintained at 37°C in a humidified 5% CO₂ atmosphere.

Microbe strains

For cloning and plasmid generation, we used the *E. coli* DH5α strain.

METHODS DETAILS

Histological analyses

Tissues were fixed in 3.7–4% paraformaldehyde (Cat. No. 252931, PanReac AppliChem), paraffin-embedded, cut in 2-3 μm sections, and stained with hematoxylin (Cat. No. 10-2332, Casa Álvarez) and eosin (Cat. No. 10-3002, Casa Álvarez). All these procedures were carried out at the Pathology Unit of our Center. Analyses of tissue sections and tumor types were blindly analyzed by a pathologist (M.C.G-M.). In the case of T-ALL, identification of tumors was based both in surface and molecular markers as indicated in the main text. Pre-pro B-ALLs were identified based on the following surface and molecular markers: Pax5⁺, c-Kit^Low, CXCR4⁺, Flt3⁺, CD24⁺, CD43⁺, B220⁻, CD19⁻, CD21⁻, CD23⁻, IgM⁻, and IgD⁻. In the case of ovarian and testicular tumors, the origin was determined by looking at the cells that become tumorigenic at incipient tumor phases (*rete ovarii* and *testis*, respectively). In the case of fibrosarcomas, the diagnosis was based on: (i) Mesenchymal hyperplasias of clear fibroblastic origin

according to histological criteria. (ii) Histological storiform features. (iii) Nodular growth pattern of tumors. (iv) Lack of hyalinization. (v) Vimentin immunostaining positive. Harderian gland tumors and papillomas were identified according to their prototypical histological features.

Immunohistochemistry

Immunohistochemical staining was performed using a Ventana Discovery Ultra instrument (Roche, Catalog No. 05987750001). Paraffin-embedded sections were dewaxed, incubated with Tris EDTA (pH 8.0) for heat-induced antigen retrieval, and incubated for 40 min with the primary antibody to vimentin (Catalog No. 347R-15, Cell Marque, 1:100 dilution). For standard staining, the Discovery OmniMap anti-Rb HRP detection system (Catalog No. 760-4311, Roche) was used for detection and hematoxylin for counterstaining.

Flow cytometry determinations

Isolated cells were washed twice in cell extraction buffer, resuspended in standard phosphate-buffered saline solution, and stained with combinations of fluorescein isothiocyanate- (FITC, Cat. No. 553729, BD Biosciences, 1:200 dilution), allophycocyanin- (APC, Cat. No. 553051, BD Biosciences, 1:200 dilution), APC-Cy7- (Cat. No. 560181, BD Biosciences, 1:200 dilution) or V500-labeled (Cat. No. 560783, BD Biosciences, 1:200 dilution) antibodies to CD4; FITC- (Cat. No. 553031, BD Biosciences, 1:200 dilution), Pacific blue- (PB, Cat. No. 558106, BD Biosciences, 1:200 dilution) or phycoerythrin-labeled (PE, Cat. No. 553032, BD Biosciences, 1:200 dilution) antibodies to CD8; APC- (Cat. No. 558643, BD Biosciences, 1:200 dilution) or PE-Cy7-labeled (Cat. No. 552880, BD Biosciences, 1:200 dilution) antibodies to CD25; APC-labeled antibodies to CD24 (Cat. No. 17-0242-82, eBioscience, 1:200 dilution); PerCP-Cy5.5-labeled antibodies to CD44 (Cat. No. 560570, BD Bioscience, 1:200 dilution), and a PE-labeled antibody to TCRβ (Cat. No. 12-5961-82, eBioscience, 1:200 dilution).

For intracellular TCRβ and ICN1 staining, cells were fixed with Cytofix/Cytoperm (Cat. No. 554714, BD Bioscience) for 10 min and stained with PE-labeled antibodies to the TCRβ (1:50) or ICN1 (mN1A, Cat. No. 552768, BD Biosciences, 1:50 dilution) for 1 hour at room temperature in phosphate-buffered saline solution supplemented with 5% fetal bovine serum and 10% saponin. For flow cytometry detection of phosphorylated intracellular proteins, cells were fixed with 2% formaldehyde, permeabilized with 90% ice-cold methanol and incubated with antibodies to phospho-ERK1/2 (p-Thr^{202} and p-Tyr^{204}, Cat. No. 4377, Cell Signaling Technologies, 1:200 dilution) and phospho-AKT (p-Ser^{473}, Cat. No. 4060, Cell Signaling Technologies, 1:400 dilution). Cells were then stained with an Alexa-648-labeled secondary antibody to rabbit immunoglobulins (Cat. No. A21443, Invitrogen, 1:500 dilution). Antibody-stained cells were run in a FACSAria III flow cytometer (BD Biosciences) and data analyzed using the FlowJo software.

Production of viral particles

In the case of transduction of bone marrow progenitors, the lentiviral vector encoding bicistronically the intracellular domain of Notch1 (ICN1) and GFP (pICN1-GFP) was gently provided by M.L. Toribio (CBMSO, Madrid, Spain). For fibrosarcoma tumor-derived cell infection, lentiviral vectors encoding *Rras2*-targeting shRNAs (TRCN0000311478, referred to in the figures as shRNA#478; TRCN0000077751, referred to in the figures as shRNA#751; TRCN0000077752, referred to in the figures as shRNA#752, and TRCN0000354089, referred to in the figures as shRNA#089) and scrambled control shRNA (TR1.5-pLKO-1-puro; Cat No. SHC001) were obtained from Sigma. To generate the viral particles, HEK293T were transfected with the lentiviral plasmids (10 μg) together with 5 μg of pMD-G and 7.5 μg of pPax2 using the JetPEI transfection reagent (Cat. No. 101-10N, Polyplus). Lentivirus-containing supernatants were collected, passed through 0.45 μm filters (Cat. No. 10462100, GE Healthcare) and stored at −80°C for up to 2 months.

Determination of mRNA abundance

Total RNA was extracted using either the NZYol (NZYtech, Catalog No. MB18501) or the RNAeasy Mini Kit (Catalog No. 74104, Qiagen) and analyzed by qRT-PCR using the Power SYBR Green RNA-to-CT 1-Step Kit (Applied Biosystems, Catalog No. 4389986) and the StepOnePlus Real-Time PCR System (Applied BioSystems, Catalog No. 4376600). Raw qRT-PCR data were analyzed using the StepOne software v2.1 (Applied Biosystems), using the abundance of the endogenous *Gapdh* and *Cypa* mRNAs as internal normalization controls. Primers used for transcript quantitation included 5′-GGACATGCAGAACA AGC-3′ (forward) and 5′-CAGTCTCATAGCTGCCCTCA-3′ (reverse) for *Notch1* cDNA; 5′-AACTGTCAGACCCTGGTGAAC-3′ and 5′-CGACAAGTGTAGCCTCCAATC-3′ for *Notch2* cDNA; 5′-ACACTGGGAGTTCTCTGT-3′ (forward) and 5′-GTCTGCTGGCATGGGA TA-3′ (reverse) for *Notch3* cDNA; 5′-GGCCAGCTGATATAATGGAGAAAA-3′ (forward) and 5′-TCCATGATAGGCTTTGATGACTT-3′ (reverse) for *Hes1* cDNA; 5′-CGAAACTCTGGTGCATAAACT-3′ (forward) and 5′-GAACCGTTCTCCTTAGCTCTCA-3′ (reverse) for *Myc* cDNA; 5′-CGTACCCCGATTCAGGTGAT-3′ (forward) and 5′-TTGAGCAGAGCTGCTACGT-3′ (reverse) for *Cdkn2a* cDNA; 5′-GTGGATGGCTTCTGACTTTG-3′ (forward) and 5′-AGGGTTGGGCCTTACGTGAACCTG-3′ (reverse) for *Rras2* cDNA; 5′-TATCTG CACTGCCAAGACTGAGTG-3′ (forward) and 5′-CTTCTTGCTGGTCTTGCCATTCC-3′ (reverse) for *Cypa* cDNA; 5′-TGGACCAA CTGCTTAGC-3′ (forward) and 5′-TCTTCTGGGTGGCAGTGATG-3′ (reverse) for *Gapdh* cDNA.

Generation of antibodies to R-RAS2

We used a synthetic peptide corresponding to the R-RAS2 C-terminus (CPPSPEPTRKEK DKKG) to immunize rabbits using the Invitrogen service. Upon immunization, the antibodies were purified using an affinity column coated with the immunizing peptide. The antibody was tittered by enzyme-linked immunosorbent assays and the specificity tested by Western blot using control and R-RAS2 knockout cells. Further experiments indicated that this antibody recognizes R-RAS2 but not R-RAS or the classical RAS proteins.

Western blotting

In the case of cells grown *in plastico*, they were washed three times with phosphate-buffered saline solution and lysed in BLYS buffer (50 mM Tris-HCl [pH 7.5], 1 mM EGTA, 1 mM EDTA, 1% Triton X-100 [Cat. No. 11332481001, Sigma-Aldrich], 1 mM Na_3VO_4, 50 mM NaF, 5 mM sodium pyrophosphate, 0.27 M sucrose, 1 mM PMSF and a cocktail of protease inhibitors [Cømplete, Cat. No. 11697498001, Roche]). In the case of mouse tissue extracts, the frozen samples were disrupted with the help of a Dispomix Drive homogenizer (Cat. No. 900020.00, Medic Tools AG) in gentleMACS M tubes (Cat. No. 130-096-335, Miltenyi Biotec) in BLYS buffer. Cellular extracts were then precleared by centrifugation at 20,000 xg for 10 min at $4°C$, denatured by boiling in $5\times$ SDS-PAGE sample buffer, separated electrophoretically, and transferred onto nitrocellulose filters (Cat. No. 2022-04-26, Thermofisher Scientific) using the iBlot Dry Blotting System (Cat. No. IB21001, Thermofisher Scientific). Membranes were blocked in 5% bovine serum albumin (Cat. No. A4503, Sigma-Aldrich) in TBS-T (25 mM Tris-HCl [pH 8.0], 150 mM NaCl, 0.1% Tween-20) for at least 1 hour and then incubated overnight with the appropriate antibodies. Primary antibodies used included those directed to R-RAS2 (homemade, see above; 1:1,000 dilution), tubulin α (Cat. No. CP06-100UG, Calbiochem, 1:2,000 dilution), phospho-ERK1/2 (p-Thr^{202} and p-Tyr^{204}, Cat. No. 4370, Cell Signaling Technology, 1:1,000 dilution), total ERK (Cat. No. 9102, Cell Signaling Technology, 1:1,000 dilution), phospho-AKT (p-Thr^{308}, Cat. No. 4056, Cell Signaling Technology, 1:1,000 dilution), phospho-AKT (p-Ser^{473}, Cat. No. 4051, Cell Signaling Technology, 1:1,000 dilution), total AKT (Cat. No. 2920, Cell Signaling Technology, 1:1,000 dilution), PTEN (Cat. No. 9583, Cell Signaling Technology, 1:1,000 dilution), the ICN1 fragment (Cat No. 4147, Cell Signaling Technology, 1:1,000 dilution), phospho-p70 S6K (p-Thr^{389}, Cat. No. 9205, Cell Signaling Technology, 1:1,000 dilution), phospho-S6RP (p-Ser^{240} and p-Ser^{244}, Cat. No. 2215, Cell Signaling Technology, 1:1,000 dilution), phospho-S6RP (p-Ser^{235} and p-Ser^{236}, Cat. No. sc-293144, Santa Cruz Biotechnology, 1:1,000 dilution), phospho-p70 S6 Kinase (Thr^{421} and Ser^{424}, Cat. No. 9204; Cell Signaling Technology, 1:1,000 dilution), total S6K (Cat. No. sc-230, Santa Cruz Biotechnology, 1:1,000 dilution), phospho-RSK (p-Ser^{380}, Cat. No. sc-377526, Santa Cruz Biotechnology, 1:1,000 dilution) and total RPS6 (Cat. No. A300-557A, Bethyl, 1:1,000 dilution). Membranes were then washed three times with TBS-T, incubated with the appropriate secondary antibody (ECL Rabbit IgG, HRP-linked whole Ab, Cat. No. NA934-1ML, Amersham, 1:5000 dilution; ECL Mouse IgG, HRP-linked whole Ab, Cat. No. NXA931-1ML, Amersham, 1:5000 dilution) for 60 min at room temperature and washed three times as above. Immunoreactive bands were visualized using a chemiluminescent method (ECL Pierce, Cat. No. 32106, Thermofisher Scientific). When quantifications were performed, the tubulin signal was used as normalization control to avoid spurious variations due to different loading of protein extracts among samples.

Cell proliferation assays

Fibrosarcoma cells and thymocytes (detached from OP9 feeder layers) were plated onto 24- and 6-well plates at a concentration of 5,000 cells/mL and 2×10^6 cells/mL, respectively. In the case of experiments using drug inhibitors, cells were treated with either inhibitors (concentrations indicated in the appropriate figure legend) or vehicle alone (DMSO). After 2 h, cells were collected, diluted in Beckman Counter ISOTON II (Cat. No. 8448011, Beckman) and counted using the Beckman Coulter Z1 apparatus.

CRISPR–Cas9-mediated gene knockouts

To knockout *Rras2* in FS#2 cells, we used the CRISPR–Cas9 approach based on the homology-directed repair (HDR) pathway. To this end, we generated two plasmids encoding the Cas9 and two synthetic sgRNAs (mTC21 sgRNA1 and mTC21 sgRNA2) targeting 25 bp regions around the start codon of the *Rras2* gene that were designed using the Benchling CRISPR design tool (www.benchling. com) (Table S2). Upon phosphorylation and annealing, each sgRNA was cloned into the BbsI-digested pX330-U6-Chimeric_BB-CBh-hSpCas9 vector (Cat. No. 42230, Addgene) to generate the pMFP23 and pMFP24 plasmids. In the case of the mTC21 sgRNA2, we mutated the PAM sequence in the pMFP24 plasmid using the primers mPAM2 mut F/R (Table S2). In addition, we generated a third plasmid containing the donor DNA required for the HDR step (pMFP34). To this end, a pBlueScript SK ii (+) vector (Cat. No. 212205, Addgene) containing the EGFP sequence was used as the backbone (pJG1). Two DNA fragments homologous to the genomic region up- (left homology arm, LHA) and downstream (right homology arm, RHA) of the ATG of the *Rras2* gene were PCR-amplified using genomic DNA from mouse FS#2 cells (Table S2). To introduce the homology fragments into the backbone, primers used to amplify the genomic DNA were provided with overhang sequences containing a HindIII/BamHI and XhoI/NheI sites for the left and right homology arms, respectively. The left and right homology arms were sequentially cloned into the backbone vector, giving rise to an insertion of a cDNA containing EGFP and polyA sequences that incorporates a frameshift in the downstream *Rras2* sequences. With this approach, we could follow and enriched the gene-edited cells by EGFP epifluorescence. Cells exponentially growing in 6 cm plates were transfected using Lipofectamine 2000 with 1.0, 1.5, 2.0 and 3.0 μg of total DNA with a 1 (for pMFP23 or pMFP24) to 2 (pMFP34) ratio. After 24 h, cells were again transfected with pMFP34 alone. 36 h after the second

transfection, EGFP-positive cells were isolated by flow cytometry using a BD FACSAria III cell sorter. Screening for the proper generation of *Rras2* knockout independent clones was carried out by Western blot.

shRNA mediated *Rras2* transcript knockdown

Fibrosarcoma tumor-derived cells (FS#2) were infected in the presence of polybrene (8 μg/mL; Cat. No. H9268-5G, Sigma-Aldrich) with lentiviruses encoding the indicated shRNAs (see above). 48 h after the transduction step, cells were subjected to puromycin selection (2 μg/mL, Cat No. P8833, Sigma-Aldrich). The proper depletion of R-Ras2^{Q72L} in cells was confirmed by immunoblotting and/or qRT-PCR.

Gene expression profiling

Total RNAs from control and *Rras2* knockout FS#2 cells were isolated using the RNAeasy Mini Kit (Catalog No. 74104, Qiagen) and analyzed using Affymetrix microarrays (Clariom^{TM} S Assay HT) at the CIC Genomics Core Facility according to the manufacture's recommendations.

Bioinformatics of microarray data

R version 3.6.3 was used for statistical analyses along with Python version 3.9.0 for text file processing. Signal intensity values were obtained from expression microarray CEL files after robust multichip average (RMA). Differentially expressed genes were identified using linear models for microarray data (limma) (Ritchie et al., 2015). Adjusted p values for multiple comparisons were calculated applying the Benjamini-Hochberg correction (FDR). Gene Ontology and KEGG pathways enrichment analyses were performed using DAVID (https://david.ncifcrf.gov) (Huang da et al., 2009; Huang-da et al., 2009). Expression heatmaps were generated using the heatmap3 R package (http://CRAN.R-project.org/package=corrplot). Volcano plots were generated using the Glimma R package (Su et al., 2017). GSEA (Subramanian et al., 2005) were performed with described gene sets using gene set permutations (n = 1000) for the assessment of significance and signal-to-noise metric for ranking genes. The gene sets used were those from the Molecular Signatures (MSigDB v7.2) and the Harmonizome databases (Rouillard et al., 2016). To evaluate the gene signature fitness of the transcriptome of FS#2 cells with expression data from fibrosarcoma and leiomyosarcoma cases contained in the Gene Expression Omnibus database (GSE2719) (Detwiller et al., 2005), the enrichment scores for both the upregulated and downregulated signatures found in control versus sh#89 FS#2 cells were calculated using single-sample GSEA (Reich et al., 2006; Subramanian et al., 2005).

IMMUNOFLUORESCENCE ASSAYS

Fibrosarcoma cells were plated onto coverslips previously incubated with fibronectin (2 μg/mL, Cat. No. 10838039001, Roche) for 1 h at 37°C in imaging buffer (20 mM HEPES [pH 7.4], 140 mM NaCl, 2.5 mM KCl, 1.8 mM CaCl$_2$, 1.0 mM MgCl$_2$). 24 h later, the cells were fixed in 4% formaldehyde (Cat. No. F8775, Sigma-Aldrich) in phosphate-buffered saline solution for 15 min, washed twice with phosphate-buffered saline solution, permeabilized with TBS-T supplemented with 0.5% Triton X-100 for 15 min, washed again three times with TBS-T, blocked in TBS-T supplemented with 2 % bovine serum albumin for 2 h, and then incubated in a wet chamber with primary antibodies to α-smooth muscle actin (Cat. No. A2547, Sigma, 1:400 dilution). Cells were then washed three times with TBS-T and incubated with either Alexa Fluor 594-labeled (Cat. No. A11032, Invitrogen, 1:400 dilution) or Alexa Fluor 488-labeled (Cat. No. A32723, Invitrogen, 1:400 dilution) goat anti-mouse IgG for 30 min at room temperature and washed twice as above. Finally, cells were then stained with 1 μg/mL of 4′,6-diamidino-2- phenylindole (Cat. No. D1306, Invitrogen) for 3 min to visualize the nuclei and images were captured in a Laser Scan Confocal Microscopy Leica SP8.

QUANTITATION AND STATISTICS

Quantitation of phosphorylation levels in immunoblot analyses

For quantification of the relative protein phosphorylation levels, the intensity of the bands was measured with the ImageJ software (National Institutes of Health, Bethesda, MD). Values were normalized taking into consideration the tubulin levels present in each sample.

Quantitation of morphological parameters of fibrosarcoma cells

Cells displaying fibers decorated with a smooth muscle cell actin were counted *de visu*. The area and roundness index of cells was calculated using the ImageJ (in the latter case, value 1 = completely rounded cell).

Statistics

Statistical analyses were carried out using GraphPad Prism software (version 6.0). The number of biological replicates (n), the type of statistical tests performed, and the statistical significance are indicated for each experiment in the figure legends as well as the results section of this document. Data normality and equality of variances were analyzed with Shapiro-Wilk and Bartlett's tests, respectively. Parametric distributions were analyzed using Student's t-test (when comparing two experimental groups) or one-way ANOVA

followed by Tukey's HSD test or Dunnett's multiple comparisons test (when comparing more than two experimental groups). Nonparametric distributions were analyzed using either Mann-Whitney test (for comparisons of two experimental groups) or Kruskal-Wallis followed by Dunn's test (for comparisons of more than two experimental groups). To test the differences in survival between two or more independent experimental groups, we used the Log-rank (Mantel-Cox) test. In all cases, values were considered significant when p $\leq$ 0.05. Data obtained are given as the mean $\pm$ SEM.